

**Searching for Spectral Signatures of the  
Hidden Secondary Component of  
BM Ori:  
Improved Spectroscopic Findings**

by

Raquel Martinez

Advisor: Dr. Seth Redfield

A thesis submitted to the  
faculty of Wesleyan University  
in partial fulfillment of the requirements for the  
Degree of Master of Arts  
in Astronomy

## Acknowledgments

First and foremost, I would like to thank my advisor Dr. Seth Redfield for the help and guidance he has given me these past two years. His notoriously high expectations and standards have challenged me but I've learned and grown so much as an astronomer because of them. Working with him, getting to know him, and being surrounded by his passion and enthusiasm for astronomy is truly inspiring.

The astronomy department here is a great, little group and they have made my studies and research at Wesleyan all the more enjoyable. From research discussion, to pizza lunch, to group meetings, to late nights typing up lab reports or theses, I feel that Van Vleck Observatory has been my home away from home. I would personally like to thank Dr. William Herbst for his leadership and willingness to provide insight and suggest avenues of inquiry regarding BM Ori. I'd like to give my appreciation to Dr. Adam Jensen for his coding assistance towards the end of my project. I also want to thank and congratulate my fellow graduating classmates Diana Windemuth and Craig Malamut for being great sounding boards for ideas and all-around pleasures to be around, no matter if it were in the classroom, down in the VVO basement, or hanging out outside of the observatory.

I'm truly grateful for all of the friends, undergraduate and graduate, I've made through Wesleyan. I'm excited for my next steps but I'm sad to leave them behind. I wish them well.

Lastly, I want to thank my family and friends back in California for all of their love and support during my time away on the East Coast. I've missed them dearly and cannot wait to go back and see them again before I head off on to my next adventure.

# Contents

<b>1</b>	<b>Introduction</b>	<b>1</b>
1.1	First Sightings . . . . .	1
1.2	BM Ori Secondary Models . . . . .	5
1.2.1	The Disk . . . . .	5
1.2.2	The Black Hole . . . . .	7
1.2.3	Dust Clouds and Possibility of Third Light . . . . .	8
1.3	Implications of BM Ori's Evolution . . . . .	9
1.3.1	Planet Formation in BM Ori's Secondary Disk . . . . .	9
1.4	This Work . . . . .	11
<b>2</b>	<b>Observations</b>	<b>13</b>
2.1	The Data Set . . . . .	13
2.1.1	Instrumentation . . . . .	13
2.1.2	Data Reduction Process . . . . .	17
2.2	Phase Sampling of BM Ori . . . . .	18
<b>3</b>	<b>Data Analysis</b>	<b>22</b>
3.1	Normalization . . . . .	22
3.1.1	Normalization of Spectra Using <code>mkfb.pro</code> . . . . .	23
3.1.2	Truncation of Normalized Spectrum . . . . .	25

3.1.3	Removal of Nebular Emission and Interstellar Absorption .	28
3.2	Telluric Line Removal . . . . .	28
<b>4</b>	<b>Results</b>	<b>30</b>
4.1	Spectral Typing of Individual Components of BM Ori . . . . .	30
4.1.1	Need for Simultaneous Fitting of Primary and Secondary Spectral Template Combinations . . . . .	32
4.1.2	Concatenation of HET Data . . . . .	36
4.1.3	Constraint of Stellar Parameters . . . . .	37
4.2	Rotational Velocity of the Components of BM Ori . . . . .	38
4.3	Refined Radial Velocity Curve . . . . .	44
4.3.1	Radial Velocity Curve via Gaussian Profile Fitting . . . . .	44
4.3.2	Radial Velocity Curve via Spectral Typing . . . . .	47
4.3.3	Eccentricity Consideration . . . . .	49
4.4	Mass Ratio . . . . .	50
<b>5</b>	<b>Fitting the Puzzle Pieces Together</b>	<b>53</b>
5.1	Summary of Results . . . . .	53
5.2	Other Idiosyncrasies of BM Ori and Future Work . . . . .	54
5.2.1	Search for Sodium Excess . . . . .	56
5.2.2	Presence of Lithium in BM Ori Spectrum . . . . .	56
5.2.3	Overabundance of Ca I 6102 Å and Ca I 6439 Å in BM Ori Spectrum . . . . .	57
5.2.4	H $\alpha$ . . . . .	58
5.2.5	Refined Spectral Typing . . . . .	60
5.2.6	Continued Observation . . . . .	61



# List of Tables

2.1	Spectroscopic Observations of BM Ori . . . . .	20
2.1	Spectroscopic Observations of BM Ori . . . . .	21
3.1	Final Line List of Possible BM Ori Absorption Features . . . . .	27
4.1	Primary Synthetic Spectra Templates Used . . . . .	32
4.2	Secondary Synthetic Spectra Templates Used . . . . .	33
4.3	Historical Summary of $T_{\text{eff}}$ found for Primary of BM Ori . . . . .	35
4.4	Historical Summary of $T_{\text{eff}}$ found for Secondary of BM Ori . . . . .	35
4.5	Primary Lines Identified and Used in Refined Radial Velocity Curve	36
4.6	Secondary Lines Identified and Used in Refined Radial Velocity Curve	36
4.7	Best-Fit Spectral Type Templates . . . . .	37
4.8	Rotation Parameters of BM Ori . . . . .	41
4.9	Comparison of BM Ori Rotation Parameters from Literature . . . . .	44
4.10	Orbital Parameters of Radial Velocity Curve Generated By Gaussian Profile Fitting Routine . . . . .	46
4.11	Orbital Parameters of Radial Velocity Curve Generated Using Spectral Typing Routine . . . . .	48
4.12	Mass Ratio of BM Ori Primary to Secondary . . . . .	51
4.13	BM Ori Orbital Parameters from Literature . . . . .	52

5.1 Sample Grid of  $\chi_r^2$  Values Obtained from Spectral Typing Routine 54

# Chapter 1

## Introduction

Nestled deep within the Orion Nebula, the eclipsing binary star system  $\theta^1$  Orionis B<sub>1</sub> (variable star designation BM Ori) is the faintest member of the four star Trapezium. The primary component is an early type star while the secondary appears to be a disk-shaped object based on the length of its eclipse. Recent photometric data have strengthened the notion that in addition to being an unconventional binary system, the disk is actively evolving (Windemuth et al. 2013). These strange features indicate that the usual binary star system model does not accurately describe BM Ori. Motivated by these data, our project seeks to explore and probe BM Ori spectroscopically at unprecedented resolution and sensitivity utilizing the 9.2 m Hobby-Eberly Telescope High Resolution Spectrograph at McDonald Observatory near Fort Davis, Texas. We begin with a historical discussion of BM Ori.

### 1.1 First Sightings

The Orion Nebula is visible to the naked eye as the second “star” of the sword in the constellation Orion. It is then no surprise that one of the first observers to scrutinize the region was Galileo Galilei. In a drawing from 1617, Galileo was able to resolve part of the Trapezium and neighboring stars using his small telescope (Galileo 1617). Huygens (1659) added further detail in sketches of the nebula in



**Figure 1.1:** Hubble Space Telescope false color mosaic of the Trapezium (Bally et al. 1998). BM Ori is the upper lefthand vertex.

his *Systema Saturnia*. Not until 1673 (by Abbe Jean Picard and independently by Huygens in 1684) was BM Ori discovered (Pope & Mosher 2006). The system and the rest of the Trapezium are clearly seen to the upper left in Figure 1.1.

Figure 1.2 shows a zoomed in picture of the BM Ori system (Close et al. 2012). Though this is a high-resolution image, the secondary component is still not visually resolved. BM Ori’s photometric variability was discerned by Goos (1918) while the eclipsing binary aspect of the system was not known until 1920 (Hartwig 1921). At that time the period of the binary was 6.4754 days. In 1940 the ephemeris was updated by Schneller (1940) to be  $JD_{min} = 2422717.342 + 6.47075E$  in addition to being designated an Algol-type eclipsing binary - that is, an eclipsing binary system whose secondary fills its Roche lobe. Schneller (1940) found the system’s maximum magnitude to be 8.1 and its eclipse depth to be 0.61 magnitudes. Also, its eclipse duration was found to last 23.5 hours. Struve & Titus (1944) confirmed Hartwig’s  $\sim 6.5$  day period via spectroscopic observations. The first light curve of BM Ori was published by Hall & Garrison

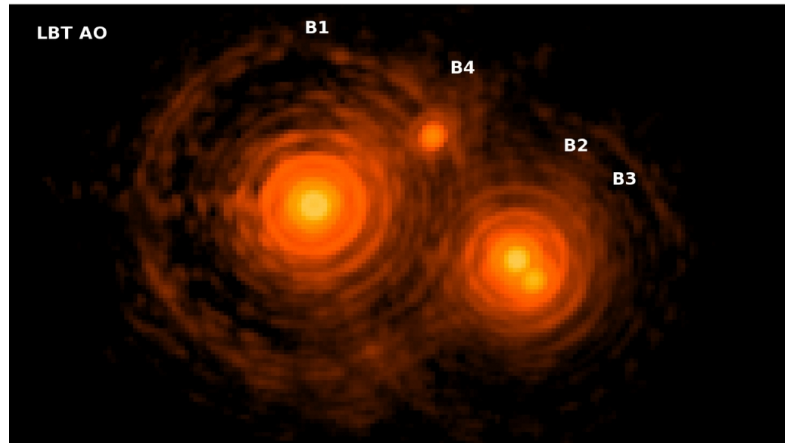


**Figure 1.2:** High-resolution, 2.16  $\mu\text{m}$  wavelength image of BM Ori using the LBT AO System. BM Ori (and its unlabeled secondary) are B<sub>1</sub> and B<sub>5</sub> in Close et al. (2012). The angular distance between B<sub>1</sub> and B<sub>2</sub> is about 1".

(1969) seen in Figure 1.3. Recent observations made by the Microvariability & Oscillations of Stars Telescope (MOST) have refined BM Ori’s ephemeris to be  $\text{JD}_{min} = 2455548.738 + 6.4705315E$  (Windemuth et al. 2013). The latest BM Ori light curve is seen in Figure 1.4.

In both of these light curves, evidence of BM Ori’s peculiar nature can be seen. “Shoulders” exist before primary ingress and after primary egress as seen in Figure 1.5. Hall & Garrison (1969) assumed the primary eclipse to be total but even so the search for the spectroscopic signature of the secondary remained elusive until the discovery of Ca II and Na I lines in BM Ori’s spectrum by Popper & Plavec (1976). See Figure 1.6 for a sample of their spectra. From their observations, Popper and Plavec published the first radial velocity curve (Figure 1.7) showing a semi-amplitude velocity of  $52.8 \pm 2.1 \text{ km s}^{-1}$  for the primary and  $171 \pm 10 \text{ km s}^{-1}$  for the secondary.

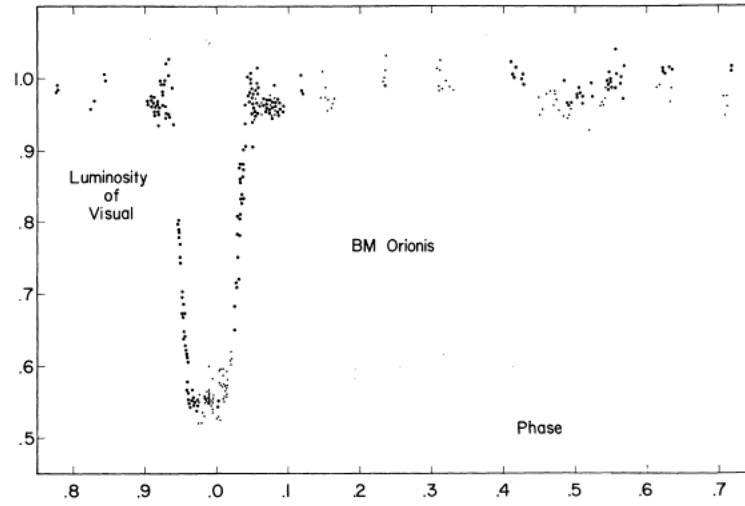


**Figure 1.3:** First published light curve of BM Ori (Hall & Garrison 1969).

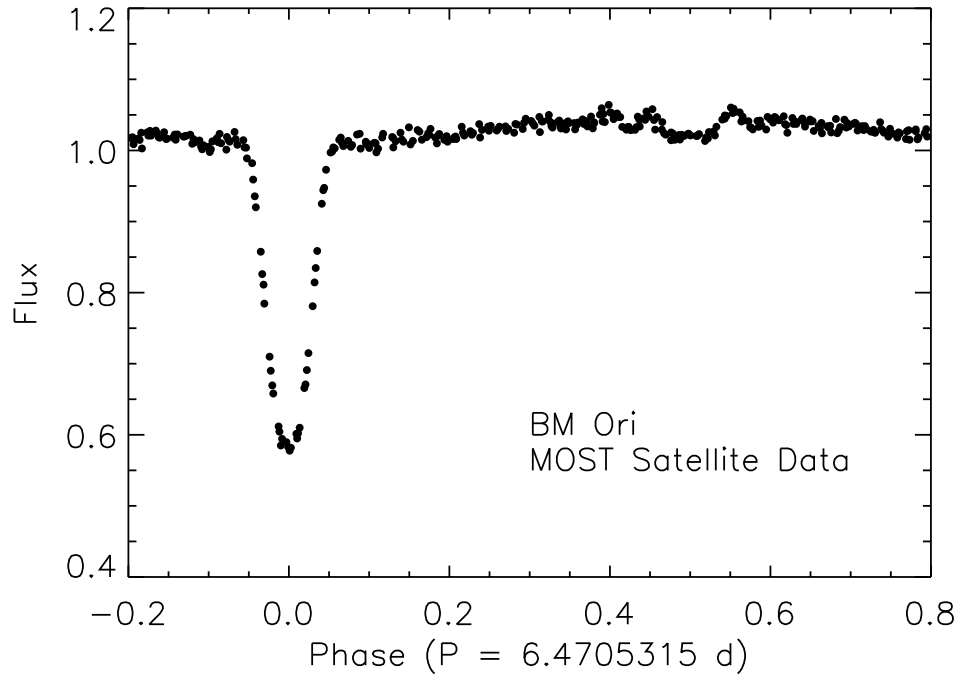


**Figure 1.4:** Recent MOST light curve (Windemuth et al. 2013). Note the impressive coverage of BM Ori's orbital phase.

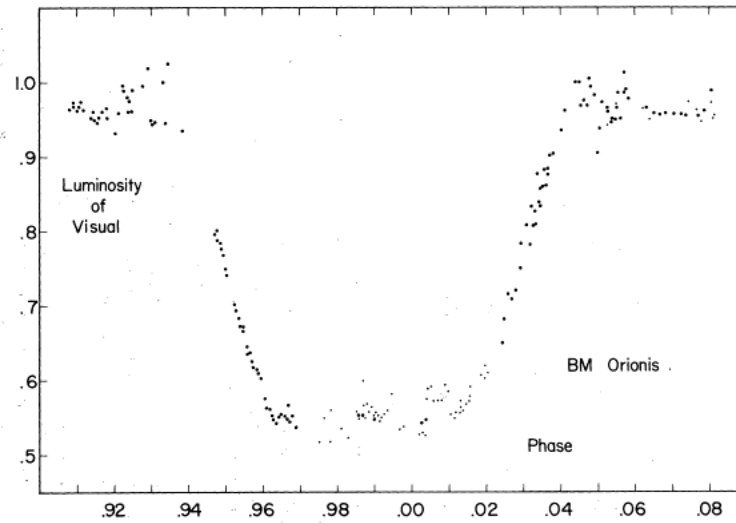


**Figure 1.5:** Light curve of BM Ori focused on primary eclipse (Hall & Garrison 1969). Note increased intensity just before ingress and just after egress.

## 1.2 BM Ori Secondary Models

The duration of BM Ori’s primary eclipse indicates that the secondary’s radius should be larger than that of the primary *if* the secondary were a spherical star. Yet, due to the fact that the luminosity observed from the system is not dominated by this secondary component nor is its spectrum easily found, creative theories and models for the physical geometry and astrophysical make-up of BM Ori have been suggested.

### 1.2.1 The Disk

A geometrically-thick and optically-thin disk has the potential to explain the length of the primary eclipse duration while preventing the secondary luminosity to dwarf that of the primary. This type of structure is necessary so that almost 50% of the primary’s light can be blocked during eclipse totality allowing for the primary spectrum to always be seen. There could very well be a star within this

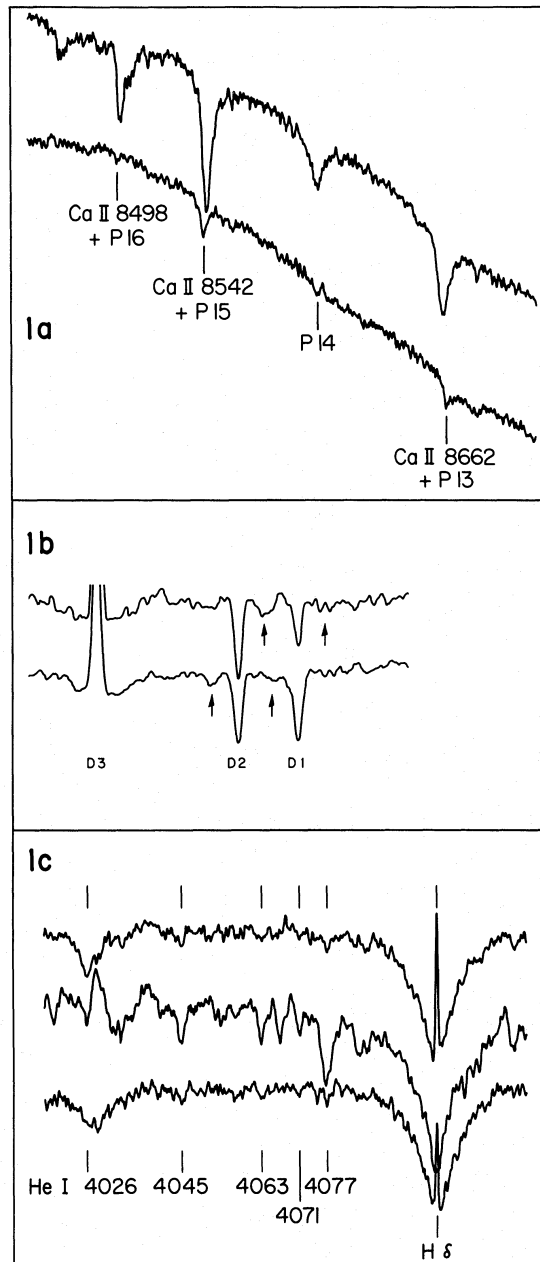


**Figure 1.6:** Sample spectra from Popper & Plavec (1976). (1a) The spectra of  $\xi$  Leo, an F0 III star, is arbitrarily offset above that of BM Ori. (1b) Sodium D line region of BM Ori's spectrum. The arrows indicate absorption features due to the secondary. Top spectrum was taken at 0.36 phase while bottom spectrum was taken at 0.65 phase. (1c) Comparison of BM Ori spectra and  $\epsilon$  Cep, an F0 IV star. Top spectrum was taken at 0.97 phase. Middle spectrum is that of  $\epsilon$  Cep. Bottom spectrum was taken at 0.98 phase.

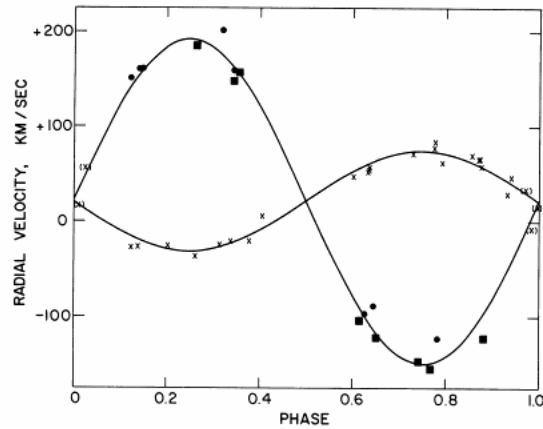


**Figure 1.7:** Radial velocity curve produced by Popper & Plavec (1976). The lines observed to generate this plot were He I from the primary and Na I from the secondary.

disk or the disk is itself an evolving pre-main sequence (PMS) star as both of these scenarios can explain the light curve seen. Antokhina et al. (1989) suggested that instead of a disk, the secondary is an oblate spheroid flattened by its own rotation (see Figure 1.8).

### 1.2.2 The Black Hole

In 1972 an even more interesting description of the BM Ori system surfaced. Wilson (1972) suggested that perhaps the secondary component of the system was a black hole surrounded by a thin disk. This disk would have a somewhat clear center making it more ring-like. In addition, through this transparent medium the primary could be continuously seen. As convenient as this scenario would be in explaining BM Ori's peculiar light curve, the probability that a black hole is in BM Ori is very small. The formation of a black hole would require some sort of remnant of scattered material in the region surrounding the system. No such material has been found. Also, the discovery of spectral features consistent with that of a star (see Fig. 1.6) have pretty much cast this theory out all together.

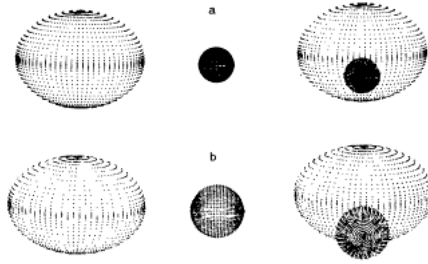


**Figure 1.8:** Proposed oblate spheroid nature of BM Ori from Antokhina et al. (1989).

### 1.2.3 Dust Clouds and Possibility of Third Light

BM Ori's wavelength-dependent light curve (Zakirov & Shevchenko 1982; Wolf 1994) lends credence to the notion that dust surrounds the cooler secondary. This idea is bolstered by the fact that disk models, as mentioned above, cannot produce the observed wavelength dependence. Bondar' & Vitrichenko (1995) actually suggested that perhaps the cooler secondary does not eclipse the star. Instead, it is dust that obscures BM Ori's primary and in fact the secondary star is a third source, all of which are contributing to the total flux observed. The failure to identify absorption features due to the secondary contributed to the credibility of this theory. More recent findings of the secondary's spectral lines have required revision to this dust cloud theory. Vitrichenko (2005) speculated that perhaps the hottest dust (i.e., closest to the hot star) was obscured during primary eclipse. Using infrared observations in the *JHKLM* bands outside eclipse and *JHKL* bands during eclipse, a complex wavelength dependence was found and best modeled by the secondary's disk and dust contributing at all phases of the orbit except during primary eclipse. The model also assumed that the secondary was partially involved in the primary eclipse.

To explain some of the shortcomings of the dust cloud theory, the idea of third light has been suggested, enabling the presence of an early-type star spectrum

during the primary eclipse. Recent imaging campaigns (Close et al. (2012); McCaughrean & Stauffer (1994)) identified at least three other stars within  $1''$  of BM Ori. Even so, none of these stars could mimic the primary's B-type spectrum during eclipse. Vitrichenko et al. (2006) concluded that a third component of BM Ori exists, but its period is far too long to alter the light curve — it can only be detected spectroscopically. Perhaps an extended envelope participates in the eclipse, but as of yet, no conclusive spectroscopic studies have confirmed this notion.

### 1.3 Implications of BM Ori's Evolution

New adaptive optic photometry and subsequent analysis from Close et al. (2012) of the Orion Trapezium Cluster showed that the  $\theta^1$  Orionis B<sub>1</sub> system is a dynamic “mini-cluster” which will almost certainly eject its low-mass members. Another source of activity is seen in the changing light curve of BM Ori over the past 40 years. This indicates that there is some opacity variation in its disk (Windemuth et al. 2013). Accreting material from BM Ori's disk onto the secondary star is a likely cause. Palla & Stahler (2001) showed that both members of BM Ori have contraction ages less than  $10^5$  years, implying that we are witnessing the system's youth and active evolution. Speculating about BM Ori's final state will be an interesting idea to consider.

#### 1.3.1 Planet Formation in BM Ori's Secondary Disk

The NASA *Kepler* mission launched a space telescope in 2009 to observe almost 150,000 main-sequence stars. One of the main goals of this mission is to find an Earth-like planet orbiting a Sun-like star. A surprising result from the wealth

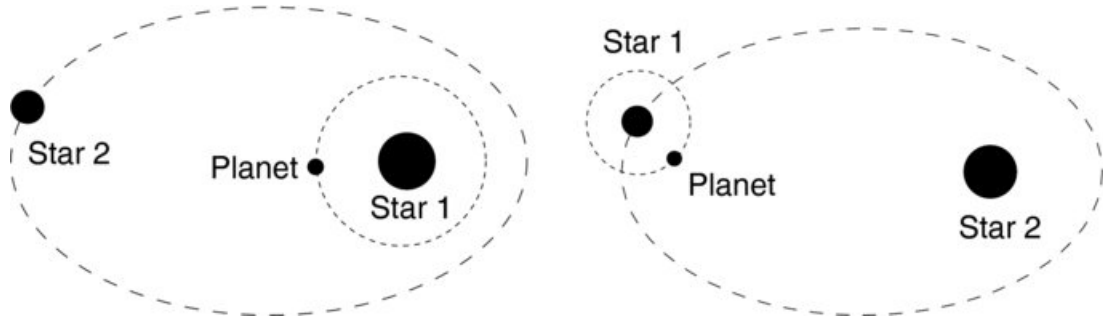


**Figure 1.9:** Example S-type I (left) and II (right) planetary orbits in binary star systems (Eggl et al. 2012).

of information coming from the telescope is the diversity of planetary systems identified in our own Milky Way. Because of this, many have questioned prevailing planet formation theory so that the variety of exoplanet-host star relationships found by Kepler can be explained. Considering that the majority of stellar objects are in multiple systems (as high as 70%; Kiseleva-Eggleton & Eggleton (2001)) it will be increasingly appropriate to contemplate the probability, stability, and habitability of planets forming in binary (and multiple) star systems.

Dvorak (1982) defined the possible planet orbits within a binary system as P-, S-, and L-types. In a P-type system, the planet orbits both stars of the multiple system. In L-types, the planet does not actually orbit any stars in the system but librates about the Lagrangian points ( $L_4$  and  $L_5$ ) of the system. If BM Ori’s disk eventually formed into a planet, its orbit would be considered an S-type II. This describes the situation where the planet orbits the less massive member of the system. The type of planet and its potential for habitability depend on a number of factors. Eggl et al. (2012) developed an analytic method to find where the so-called “habitable zone” would be for binaries with S-type planet orbits. This method mostly considered the second star’s flux contribution and binary eccentricity for determination of the habitable zone. Cuntz (2013) implemented

an additional constraint that incorporated the orbital stability of the system in consideration of the habitable zone. In both studies, the cases considered differed from BM Ori in that the multiple systems had wide separations ( $>20$  AU). Even so, the conditions presented in the aforementioned papers almost certainly can be scaled down for “back-of-the-envelope” calculations.

The young BM Ori system may be on its way to forming a planet. Estimating the mass this planet might have, the flux it would receive from its host stars, and its chance of habitability requires knowledge of BM Ori’s stellar parameters. Also needed are the system’s orbital parameters, all of which we hope to measure in this project.

## 1.4 This Work

In an effort to better understand the components of this system, we have obtained 53 high-resolution ( $R \equiv \frac{\lambda}{\Delta\lambda} = 120,000$ ) spectra taken with the 9.2-meter Hobby-Eberly Telescope gathered over a span of 65 days in late 2008 and early 2009. In addition to being some of the highest signal-to-noise data ever taken of BM Ori, these spectra offer excellent coverage of BM Ori’s  $\sim 6.47$  day period, including ingress and egress of the primary transit and secondary minimum.

The spectral type of BM Ori as a B3 star on or near the zero age main sequence (ZAMS) was most recently updated and established by Vitrichenko & Klochkova (2001). With that said, the spectral type of the secondary has never been as well characterized. From literature, the spectral types to which the secondary component of BM Ori has been assigned have ranged from F2-G2III (Vitrichenko & Klochkova 2001; Vitrichenko & Plachinda 2000). Most of the uncertainty arises from the specific stellar models used for spectral typing and the exact range of

---

wavelengths observed. In this work, we attempt to further refine the spectral type of BM Ori.

We also search for any anomalous spectral signature of the secondary, such as excess Na I gas absorption due to the transit of a circumstellar disk. In addition, we have detected variability in the H $\alpha$  line profile and attempt to characterize its behavior. We have also identified He lines of the primary and numerous metal lines of the secondary, including Mg I, Sc II, and Li I. We will present the results of a full spectral analysis, including a refined radial velocity curve, newly constrained mass ratio, and other basic stellar parameters (e.g.  $T_{\text{eff}}$ ,  $v \sin i$ ) for both components of this youngest known binary system.

# Chapter 2

## Observations

Previous spectroscopic studies of BM Ori have focused on the optical regime, especially the primary's He I 5875.621 Å line and the secondary's Na I doublet lines at 5895.9242 Å and 5889.951 Å. This project gives a more comprehensive analysis of the full optical range (4035 Å to 7995 Å) in an effort to observe excess metal absorption of a circumstellar disk surrounding the secondary. The assumed cooler nature of the secondary will also fruitfully manifest itself in the identification of numerous metallic species expected in the optical range, as will be discussed in a later section.

### 2.1 The Data Set

#### 2.1.1 Instrumentation



**Figure 2.1:** Outside view of the HET Telescope at McDonald Observatory.

All data were taken with the 9.2-meter Hobby-Eberly Telescope (HET; Ramsey et al. 1998) High Resolution Spectrograph (HRS; Tull 1998) located at the McDonald Observatory near Ft. Davis, Texas (Figure 2.1). The HET's primary mirror utilizes 91 one-meter-sized hexagonal mirrors that form a spherical surface with a radius of curvature of 26.164 meters. The mirror segments are computer controlled so that the primary mirror can reach a maximal diameter of 11 meters. The area of the mirror is 77.6 square meters while the focal length of the telescope is 13.08 meters. The HET is permanently fixed at an altitude of  $55^\circ$  but allowed to rotate a full  $360^\circ$ . Though the primary mirror is fixed, a moving optical package follows astronomical objects as they move across the sky. This tracker contains spherical aberration correction optics. The declination range of the telescope is from  $-10^\circ 20'$  to  $71^\circ 40'$ . This allows for approximately 81% of the sky to be observed. The telescope's tracking abilities enable it to completely track this sky in as little as 0.75 hours.

The light collected by the primary mirror is led into one of three spectrographs housed at the HET. The spectrographs differ in resolution capabilities. The resolving powers of the low and medium resolution elements (LRS and MRS, respectively) range from 600 to 7000. High resolution spectra of BM Ori were obtained to search for its elusive secondary lines. The HET HRS has spectral resolution ranging from  $R = 30,000$  to 120,000; these data were collected using the spectrograph's highest resolving power of 120,000.

Observations of BM Ori were obtained over the course of 65 days beginning December 23, 2008, and ending February 25, 2009. On 18 nights during these 65 days, three consecutive 200-second exposures were taken of BM Ori. Example raw images of the CCDs are shown in Figures 2.2 and 2.3. Unfortunately, one of the 54 exposures was of the wrong target, as determined by a drastically different

observed spectrum, ultimately leaving 53 spectra available for detailed analysis.

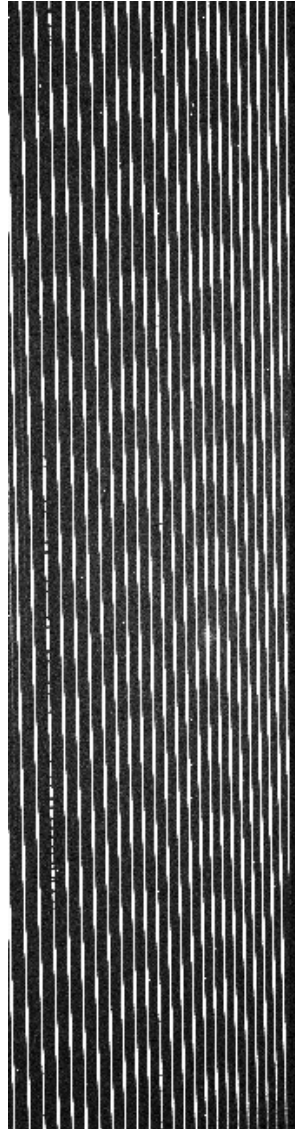


**Figure 2.2:** Raw Data from CCD 1 of BM Ori obtained on January 11, 2009. Counts ranged from 0 to  $> 10,000$ . Atmospheric molecular absorption bands in the  $7000 \text{ \AA}$  range can be seen in the third vertical column from the left.

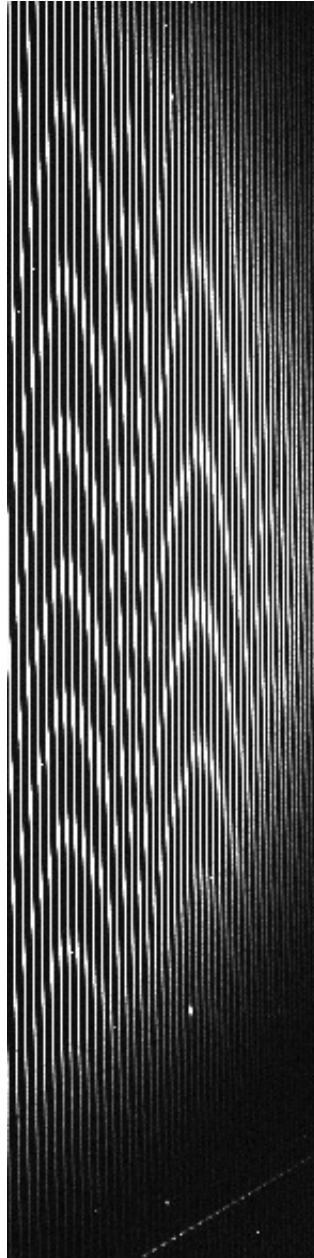


**Figure 2.3:** Raw Data from CCD 2 of BM Ori obtained on January 11, 2009.

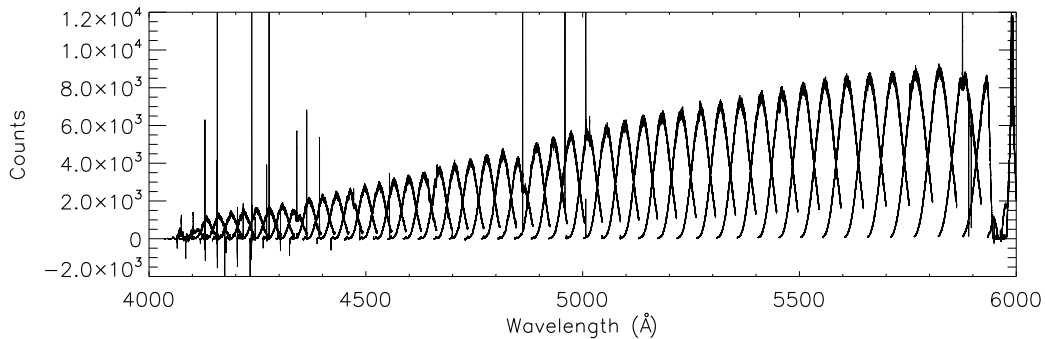


**Figure 2.4:** Reduced Data of BM Ori obtained on January 10, 2009.

### 2.1.2 Data Reduction Process

To begin a night of HET observations, bias, and flat field images are obtained. These master calibration images are used to remove the bias levels of each CCD, flatten their fields, and remove cosmic and stray light contamination. Thorium-Argon lamp exposures are used for wavelength calibration purposes. When scientific data are collected with the HET HRS, the images are focused onto a mosaic of two CCD chips. The raw HET HRS spectra from these chips are reduced using standard Image Reduction and Analysis Facility (IRAF; Tody 1993) procedures with one dimensional spectra extracted and saved as two separate files for easy access and manipulation in Interactive Data Language (IDL). Each file contained three two-dimensional arrays with wavelength, flux, and  $1\sigma$  error information for each order on the CCD chip. Final reduced data from CCD chip 2 is seen in Figure 2.4. Each file contained half of the spectral range, either 4035 Å to 6034 Å (“blue chip”) or 5934 Å to 7994 Å (“red chip”). To make the data set more manageable, the HET HRS utilizes an R-4 (blaze angle equals  $\sim 76$  degrees) echelle mosaic with cross-dispersing gratings to separate the spectral orders. Each  $\sim 2000$  Å range was broken up into smaller segments of roughly 100 Å across.

Estimation of the signal-to-noise ratio (SNR) for each exposure required identifying a “clean” portion of each order extracted from each chip and dividing its maximum flux in counts by its error, also in counts. The particular portion of the order needed to be unobstructed by absorption features from either member of BM Ori, any nebular emission or interstellar absorption features, or other CCD defects. Table 2.1 lists the exposure number, Julian Date (JD; between Dec. 23, 2008 and Feb. 25, 2009), phase, and typical signal-to-noise ratio information for all the data obtained from the HET HRS.

## 2.2 Phase Sampling of BM Ori

In Figure 2.5, recent observations by the Microvariability and Oscillations of STars Satellite (MOST; Walker et al. 2003) of BM Ori are overplotted with the phased exposures taken by the HET. The MOST observations were obtained between December 13, 2010 and January 9, 2011 (Windemuth et al. 2013). As indicated by Figure 2.5, spectra were taken during ingress and egress as well as during the secondary minimum.

The sampling of primary ingress and egress might enable us to probe the disk surrounding BM Ori. In addition, the secondary eclipse is probed meaning that we might be able to constrain the primary’s spectral type more definitively by close examination of this phase. The vicinity of the “shoulders” of both primary and secondary eclipse are spectroscopically probed and may manifest itself in absorption excess of metallic lines like Na I and Ca I.

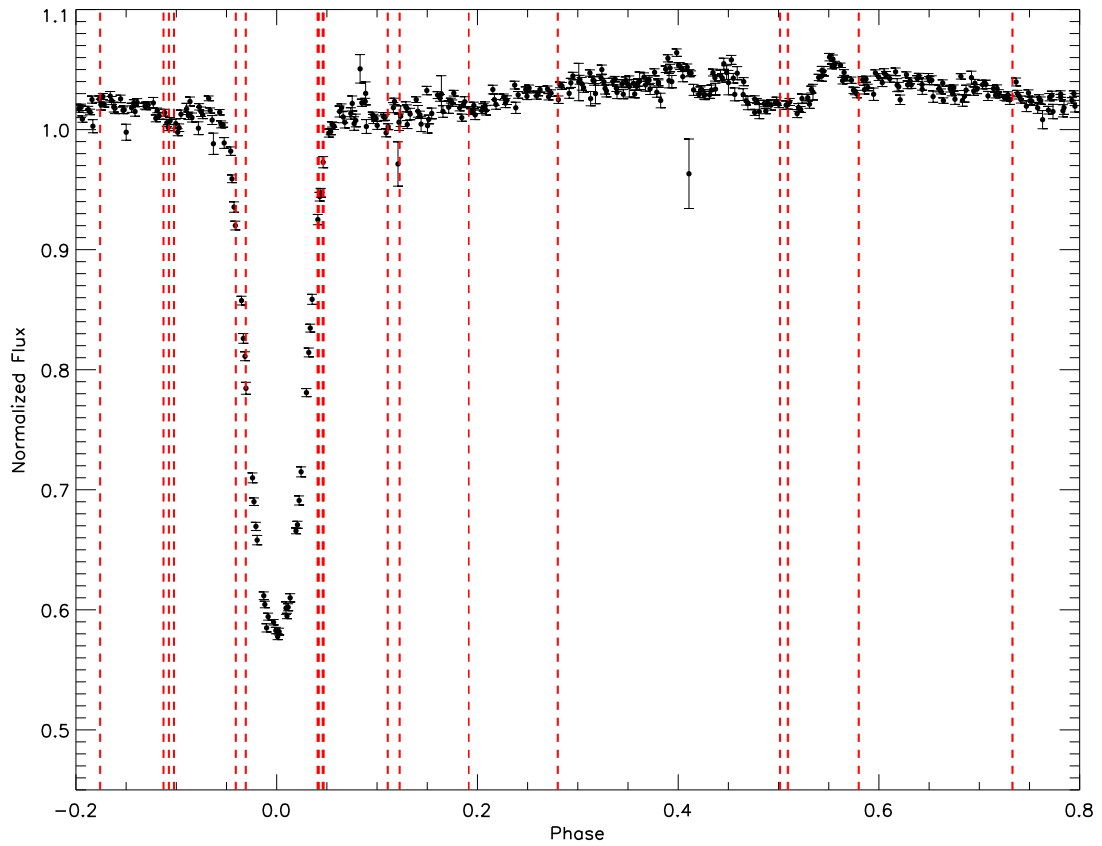


**Figure 2.5:** HET exposures are phased and plotted (red dashed lines) on top of most current light curve for the BM Ori system. Photometric data were taken by the MOST satellite in 2010 (Windemuth et al. 2013).

Table 2.1. Spectroscopic Observations of BM Ori

Exposure #	JD (2,454,800+)	Phase <sup>a</sup>	S/N <sup>b</sup>
910689	23.771	0.9587	46
910690	23.774	0.9592	43
910691	23.777	0.9597	39
910799	24.751	0.1102	46
910800	24.754	0.1106	49
910801	24.757	0.1111	48
911262	30.769	0.0402	82
911263	30.772	0.0407	89
911264	30.776	0.0413	82
911350	31.745	0.1911	74
911351	31.749	0.1917	52
911917	40.728	0.5794	33
911918	40.731	0.5798	29
911919	40.734	0.5803	24
912011	41.719	0.7325	82
912012	41.723	0.7332	78
912013	41.726	0.7336	67
912097	42.717	0.8868	82
912098	42.720	0.8872	77
912099	42.723	0.8877	60
912231	43.717	0.0413	60
912232	43.721	0.0419	52
912233	43.724	0.0424	47
912469	46.692	0.5011	102
912470	46.695	0.5016	100
912471	46.698	0.5020	99
913319	56.684	0.0453	95
913320	56.687	0.0458	85
913321	56.694	0.0469	75
913860	62.659	0.9687	81
913861	62.662	0.9692	84
913862	62.665	0.9697	80
913999	63.651	0.1221	85
914000	68.654	0.1225	92

Table 2.1 (cont'd)

Exposure #	JD (2,454,800+)	Phase <sup>a</sup>	S/N <sup>b</sup>
914001	68.657	0.1230	92
914327	68.634	0.8922	73
914328	68.637	0.8926	65
914329	68.640	0.8931	72
914403	69.630	0.0461	68
914404	69.634	0.0467	61
914405	69.637	0.0472	68
914543	72.623	0.5086	106
914544	72.628	0.5094	117
914545	72.632	0.5100	108
914844	77.611	0.2795	57
914845	77.614	0.2800	69
914846	77.617	0.2805	78
914973	81.608	0.8972	90
914974	81.611	0.8977	82
914975	81.614	0.8982	71
915317	87.602	0.8236	72
915318	87.606	0.8242	63
915319	87.609	0.8247	59

<sup>a</sup>Phase calculated using ephemeris of Windemuth et al. (2013)

<sup>b</sup>SNR calculated @ 5820 Å

# Chapter 3

## Data Analysis

Various procedures were developed to ascertain the wealth of information contained within the reduced HET data set. Artifacts of the HRS instrument and data extraction methods could have been left behind in the reduced data. In addition, the particular line of sight from Earth to BM Ori probed cold, interstellar clouds and even our own atmosphere, which manifested itself as deep, thin absorption features. Also, the Orion Nebula is a hotbed of young stellar activity which resulted in strong emission lines encroaching on regions of interest in the data set.

### 3.1 Normalization

Although reduced, the spectra still maintained the characteristic blazed intensity profile. This arises from the tilted nature of the diffraction grating on the HET HRS. This tilt scatters incident light into a preferred direction such that the intensities of wavelengths centered in each individual order are higher when compared to those at the edge of the order. The blaze artifact present in all orders of the data required a normalization procedure so that an accurate gauge of the depth and centroids of any observed spectral features could be obtained.

### 3.1.1 Normalization of Spectra Using `mkfb.pro`

Normalizing the blazed spectra required the use of the IDL program `mkfb.pro` written by Seth Redfield. This continuum normalization routine contained different normalization technique options. For this project, an eighth-order polynomial was initially assumed and the best-fit function that conformed to the reduced blazed data was found. For any identified order of interest, the reduced spectra were divided by this best-fit polynomial so that a normalized intensity of 1 resulted.

To ensure absorption features from the primary or secondary star were not normalized out of the spectra, `mkfb.pro` contains a mode that enables the user to choose segments so as not to incorporate them in the least-squares fit. Though the signal-to-noise ratio for our data was high, the secondary features were sometimes too weak to be spotted visually due to their low equivalent widths when compared to that of the primary. This required identifying hypothetical spectral lines that could be observed once normalization was done using the best guess as to the spectral type of the secondary. Most recently, Vitrichenko & Klochkova (2001) estimated BM Ori's secondary component to be that of an F2 type star. Using the synthetic spectra from Lobel (2008), around 15 lines of the primary B3 star were identified along with upwards of 50 potential secondary lines.

The author developed a procedure that automated the normalization process in addition to simultaneously converting and storing arrays of the data in velocity space using the Doppler shift formula

$$v = \frac{(\lambda_{obs} - \lambda_{rest}) * c}{\lambda_{rest}} \quad (3.1)$$

where  $\lambda_{obs}$  is the wavelength array of the reduced data order,  $\lambda_{rest}$  is the NIST

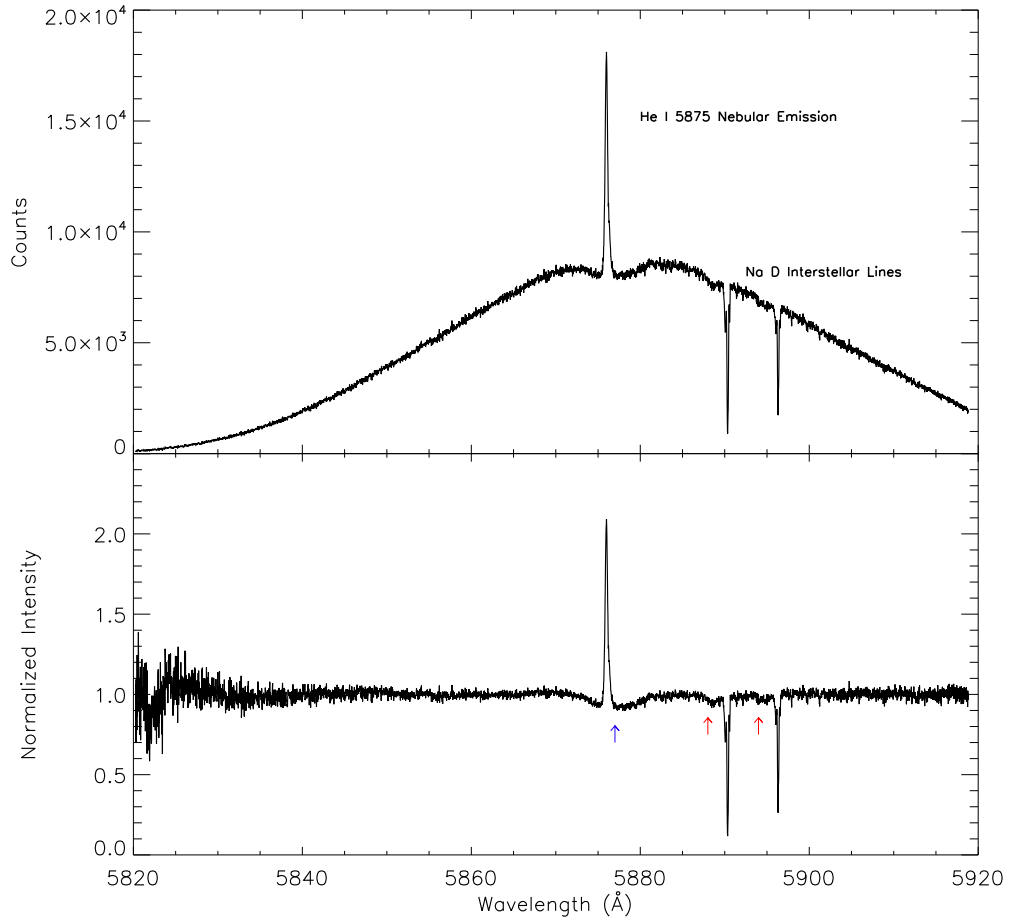


**Figure 3.1:** Single order before and after normalization using `mkfb.pro`. This particular order contains a nebular emission line at He I 5875Å and interstellar absorption in the Na I D line region. In the bottom panel, the blue arrow indicates an absorption feature of the primary star while the red arrows indicate Na I D absorption by the secondary star. The increased noise near 5820 Å is an artifact of how `mkfb.pro` attempted to fit the low counts near the edge of the order.

rest wavelength of the particular line of interest (Kramida et al. 2012), and  $c$  is the speed of light. The zero-point of the array was based on the rest wavelengths of lines predicted to be within each order. At first glance, this process seemed like a viable normalization process as a method for finding radial velocity information as can be seen in Figure 3.1. Strong features maintained their continuum level of 1, however weaker features had non-unity continuum levels or were normalized out completely. To remedy this, another normalization step seemed to be required but an alternative truncation and normalization scheme was developed to obviate the need for such a two-step process.

### 3.1.2 Truncation of Normalized Spectrum

The 4 strongest primary and 23 strongest secondary features (see Table 3.1) as determined by the initial normalization procedure described above were used in the new automated process. Unnormalized, reduced data with absorption features were converted to velocity space using the Doppler shift formula (Eq. 3.1) but this time only a buffer of  $\pm 500$  km s<sup>-1</sup> of the velocity space array was used in the polynomial fit for normalization. Using a preliminary radial velocity curve created by an initial assessment of the HET data and a best-fit sine function to this curve, an estimate for where the centroid of the absorption feature should be in the velocity array was found. An additional buffer ( $\pm 250$  km s<sup>-1</sup> for the primary and  $\pm 100$  km s<sup>-1</sup> for the secondary) was used to extract the potential stellar line information so that its information would be safe from being lost due to division by the best polynomial fit.

This procedure was done for all lines for polynomials ranging in order from 1 to 10. Once a best-fit polynomial was found for each iteration, the reduced (and truncated) flux data were divided by this result normalizing all intensities to 1 (see Figure 3.2). The author visually inspected the results and chose the appropriate normalization order, ensuring that the least amount of stellar information was divided out of the spectrum.

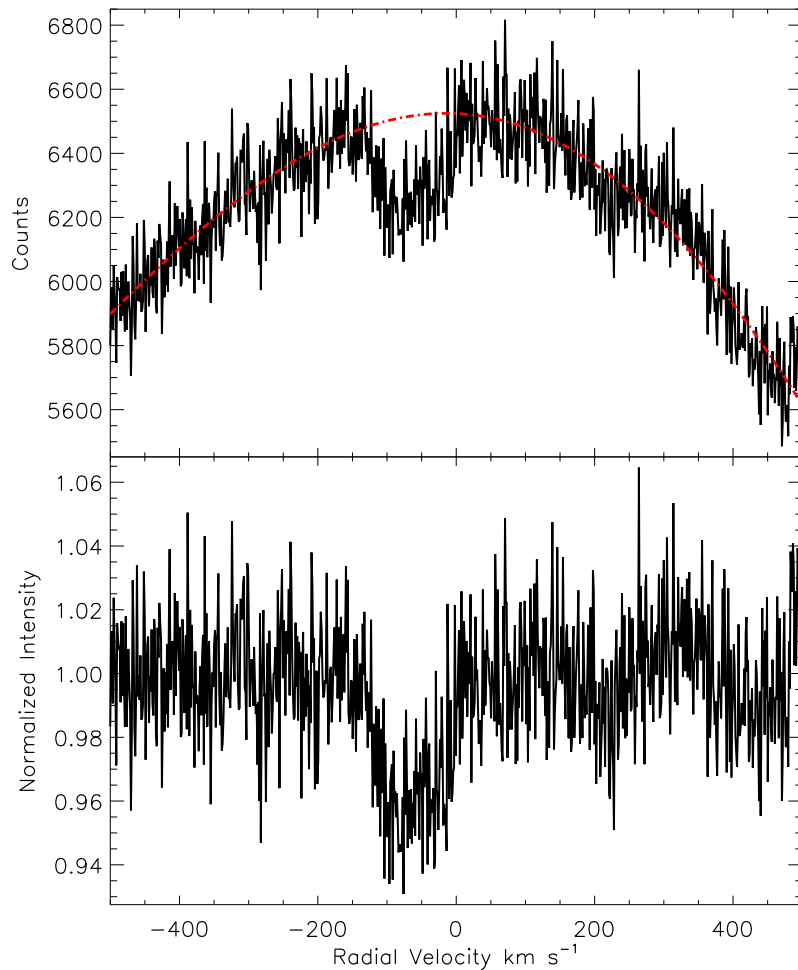


**Figure 3.2:** Mg I 5183 Å line reduced, truncated data (top) and normalized, truncated spectra. Example given is normalized by 4th order polynomial (red-dashed line).

Table 3.1. Final Line List of Possible BM Ori Absorption Features

Component	Element	Ion	$\lambda_{rest}$ ( $\text{\AA}$ )
s	Ti	I	5064.652
s	Mg	I	5183.6042
s	Ti	II	5226.5385
s	Fe	I	5226.862
s	Fe	I	5227.1503
s	Fe	I	5227.1891
s	Fe	II	5316.231
s	Fe	I	5455.6092
s	Fe	I	5462.9591
s	Fe	I	5463.2759
s	Fe	I	5615.6435
s	Fe	I	5655.49
s	Sc	II	5657.907
s	Sc	II	5658.362
s	Fe	I	5658.5313
s	Fe	I	5658.8160
s	Na	I	5889.950954
s	Na	I	5895.924237
s	Ca	I	6102.72
s	Fe	I	6191.558
s	Ca	I	6439.07
s	Li	I	6707.76
s	Li	I	6707.91
p	He	I	5875.621
p	He	I	6678.151
p	O	I	7771.94
p	O	I	7774.17

### 3.1.3 Removal of Nebular Emission and Interstellar Absorption

While not all of BM Ori's spectral features were intruded upon by nebular emission and interstellar absorption, some very important lines needed to be dealt with so as to remove these extra features to obtain the most accurate radial velocity fitting. In Figure 3.1, examples of both nebular emission and interstellar absorption are present. The author incorporated into the above normalization and truncation routine a feature that queried the user if the spectra of interest had such features present. Based on user input, the beginning and ends of these features were determined and those subsections of the data were not involved in the polynomial fitting, allowing for a more accurate representation of the continuum.

## 3.2 Telluric Line Removal

A few areas of interest were greatly affected by water vapor present in the Earth's atmosphere. The Na I doublet region is littered with sharp water vapor signatures. This common obstacle of ground-based observing was handled by computer extraction. First, to ensure the vapor features did not affect the normalization, a sigma-clipping routine was inserted into the first truncation/normalization process for only the Na I doublet lines. The sigma-clipping was only for deviations below the continuum so as to not remove noise from above. The sharp and sometimes deep features were therefore minimally able to affect the polynomial normalization functions returned in the truncation/normalization process. The next step involved knowledge of the atmospheric water spectrum. Using an IDL program developed by S. Redfield entitled `h2ofit.pro`, the author adapted this

code so that all nights' and exposures' data would be checked for water vapor signatures. The known spectra of water vapor over the spectral range 5890 to 5995 Å is effectively overlaid on the normalized spectra of BM Ori. The template is then allowed to shift and be scaled to minimize the  $\chi^2$  statistic. Once a suitable fit is found, the normalized data is divided by this shifted and scaled template as seen in Figure 3.3.

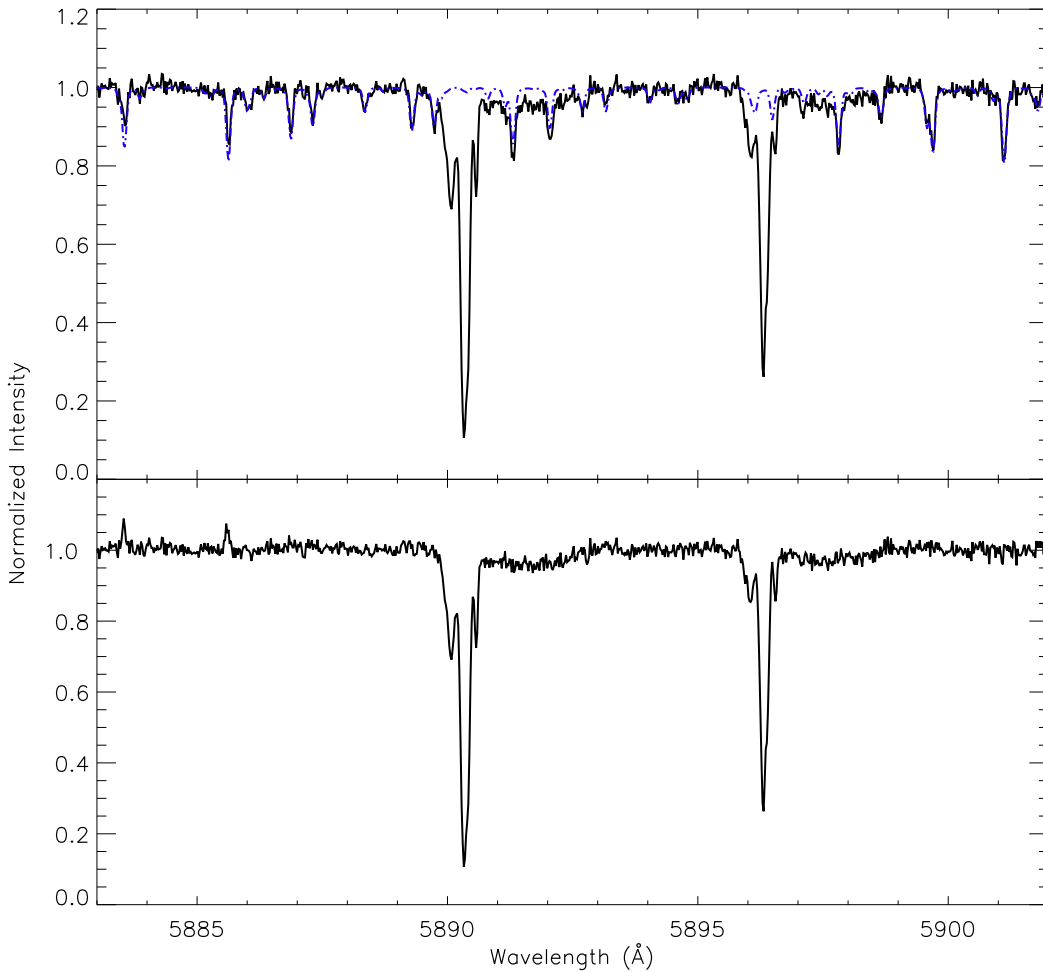


**Figure 3.3:** Single exposure before and after water vapor removal using adapted `h2ofit.pro`. The dash-dot blue line is the H<sub>2</sub>O spectrum.

# Chapter 4

## Results

Once the HET data were filtered, normalized, and truncated appropriately, substantial scientific interpretation could begin. Curve fitting and function optimization performed in this project utilized `mpfitfun.pro` and `mpfitexpr.pro` written by Markwardt (2009). The `mpfit` package is a non-linear least squares optimization routine that is more robust than IDL's `curvefit` procedure, allowing for the fixing and bounding of parameters.

The enigmatic nature of the BM Ori system had the author initially attempting to probe one particular facet of the secondary (the disk) but by the conclusion of this project, many other questions about the system were formed and here preliminary answers are given regarding the system's component spectral types, radial velocity, and mass ratios. First we discuss the process that attempted to identify the spectral type of both the primary and secondary stars of BM Ori.

### 4.1 Spectral Typing of Individual Components of BM Ori

A robust and physical representation of a stellar absorption line feature is that of a Voigt profile, or more specifically, a Gaussian profile convolved with a Lorentzian profile. The physical phenomena that contribute to the final appear-

ance of a spectral line are processes such as thermal broadening and turbulence. Given the rapid rotation measured of BM Ori’s primary star of  $>150 \text{ km s}^{-1}$  (Vitrichenko et al. (1996); Abt et al. (1970)) and secondary star of  $>50 \text{ km s}^{-1}$  (Vitrichenko & Plachinda (2000)), stellar rotational broadening was considered to be a dominant factor in the line appearances of this data set. Generation of a sophisticated, stellar atmosphere model was outside the scope of this project. Instead, the author developed a routine that took existing models, broadened them, and compared them to the data set to find the best fit. The  $v \sin i$  of both the primary and secondary was determined by convolving template spectra with the function

$$G(\Delta\lambda) = G(v) = \frac{2(1 - \varepsilon)[1 - (v_z/v_L)^2]^{1/2} + \frac{1}{2}\pi\varepsilon[1 - (v_z/v_L)^2]}{\pi v_L(1 - \varepsilon/3)} \quad (4.1)$$

where  $\varepsilon$  is the limb-darkening coefficient,  $v_z$  is the z-component of the star’s rotational velocity (toward or away from the observer), and  $v_L$  is the maximum z-component velocity the observer would see at the disk points on the limb of the star (Gray 2008). Using `mpfitfun.pro` the author created a program that attempted to identify the  $v \sin i$  that best fit the HET HRS data. The synthetic spectra used were developed by Bertone et al. (2008). Their expansive library of synthetic spectra spans the wavelength range from 3500 to 50000 Å. The  $T_{\text{eff}}$ ,  $\log g$ , and  $[\text{Fe}/\text{H}]$  combinations used for the primary and secondary stars of BM Ori are shown in Tables 4.1 and 4.2, respectively. The files listed are named via the BLUERED convention which is as follows: `tXXXXXX` is temperature in Kelvin, `gXX` is  $\log g$  of X.X, `mXX` is  $[\text{Fe}/\text{H}]$  of  $-X.X$  compared to solar abundance, and `pXX` is  $[\text{Fe}/\text{H}]$  of  $+X.X$  compared to solar abundance. Using Equation 4.1 as the

Table 4.1. Primary Synthetic Spectra Templates Used

BLUERED Filename
t17000g40m10
t17000g40m03
t17000g40p00
t17000g50m10
t17000g50m03
t17000g50p00
t20000g40m10
t20000g40m03
t20000g40p00
t20000g50m10
t20000g50m03
t20000g50p00

kernel to convolve with synthetic spectra, `mpfitfun.pro` took in each line’s wavelength and flux array, varied  $v_z$  (i.e.,  $v \sin i$ ) and the radial velocity shift, then returned the best-fit parameters.

#### 4.1.1 Need for Simultaneous Fitting of Primary and Secondary Spectral Template Combinations

In order to compare our HET data with synthetic spectra, guesses as to the stellar parameters of both the primary and secondary stars were required. Simultaneous fits were necessary due to the dilution of BM Ori’s absorption features from the combined fluxes of both stars.

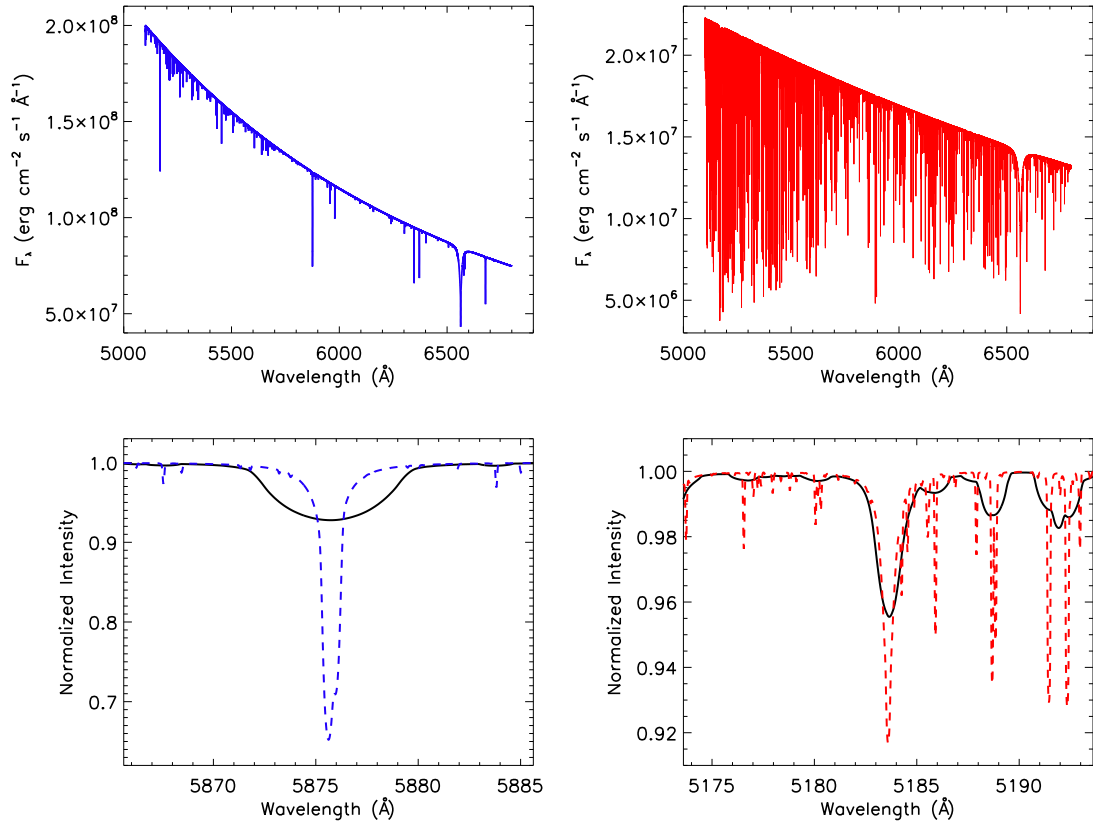
Figure 4.1 shows a few of the issues that occurred during the analysis of the BM Ori system. First, the ability to identify lines of the primary in the HET data set was made difficult by the lack of strong lines in early type stars and the need

Table 4.2. Secondary Synthetic Spectra Templates Used

BLUERED Filename
t07000g30m10
t07000g30m03
t07000g30p00
t07000g40m10
t07000g40m03
t07000g40p00
t07000g50m10
t07000g50m03
t07000g50p00
t07500g30m10
t07500g30m03
t07500g30p00
t07500g40m10
t07500g40m03
t07500g40p00
t07500g50m10
t07500g50m03
t07500g50p00

for these lines to be located at the peak blaze of each order. In addition, although the number of secondary lines is much greater than the primary lines, they were greatly diluted by the flux of the primary when normalized to the total continuum flux of the two stars.

Two effective temperature parameters per component were chosen for the spectral typing process. These temperatures were representative of published values from other analyses of BM Ori (see Tables 4.3 and 4.4). For the primary, temperatures of 17,000 K and 20,000 K were used while for the secondary, temperatures of 7,000 K and 7,500 K were used. There are future plans to obtain more fits with different stellar parameters, such as using temperatures of 18,000 K and 19,000 K



**Figure 4.1:** Example synthetic spectra for the primary and secondary stars of BM Ori from Bertone et al. (2008). Blue represents the hotter primary, red represents the cooler secondary, and black represents the co-added flux of both stars. Upper left panel shows unnormalized flux information for the primary. Upper right panel shows unnormalized flux information for the secondary. Bottom left panel shows pre-broadened spectra (dashed) overlaid on top of broadened spectra ( $\sim 188 \text{ km s}^{-1}$ ;  $\sim 44 \text{ km s}^{-1}$ ) for a strong primary feature (He I 5875 Å). Bottom right panel shows pre-broadened spectra (dashed) overlaid on top of broadened spectra for a strong secondary feature (Mg I 5183 Å).

Table 4.3. Historical Summary of  $T_{\text{eff}}$  found for Primary of BM Ori

Authors	$T_{\text{eff}}$ (K)
Al-Naimiy & Al-Sikab (1984)	22000
Vitrichenko et al. (1996)	19300
Vitrichenko & Tsymbal (1996)	<20000
Vasileiskii & Vitrichenko (2000)	17000
This work	17000

Table 4.4. Historical Summary of  $T_{\text{eff}}$  found for Secondary of BM Ori

Authors	$T_{\text{eff}}$ (K)
Popper & Plavec (1976)	7000-8000
Al-Naimiy & Al-Sikab (1984)	9500
Vitrichenko & Larionov (1996)	7000
Vitrichenko et al. (1996)	10400
Vasileiskii & Vitrichenko (2000)	5700
Vitrichenko & Klochkova (2001)	7300
This work	7000

templates from Bertone et al. (2008) so that a more continuous parameter space can be assessed. The sheer amount of secondary lines that are being fit necessitate increased values and gradations of temperature,  $\log g$ , and  $[\text{Fe}/\text{H}]$  in order to come to a firmer conclusion about the spectral type of the secondary.

Using the vast synthetic spectra library created by Bertone et al. (2008), a total of 12 primary templates were paired with 18 secondary templates for a combined parameter space of 216 stellar parameter combinations. In addition, since each exposure (53) had to be assessed, a total of 11,448 fits needed to be generated. The computing time necessary to make these fits resulted in the relatively limited sample of stellar parameters used.

Table 4.5. Primary Lines Identified and Used in Refined Radial Velocity Curve

Element	Ion	$\lambda_{rest}(\text{\AA})$
He	I	5875.621
He	I	6678.151

Table 4.6. Secondary Lines Identified and Used in Refined Radial Velocity Curve

Element	Ion	$\lambda_{rest}(\text{\AA})$
Mg	I	5183.6042
Sc	II	5658.362
Na	I	5889.950954
Na	I	5895.924237
Ca	I	6102.72
Fe	I	6191.558
Ca	I	6439.07
Li	I	6707.76
Fe	I	5226.862
Fe	I	5462.9591

### 4.1.2 Concatenation of HET Data

Any data that were to be compared against the synthetic templates of Bertone et al. (2008) needed to first be “stitched” together. The absorption information contained within the original reduced data arrays was extracted and assembled together as one piece. Tables 4.5 and 4.6 list the lines ultimately used. These lines represent the best lines that would provide the most precise information about the BM Ori system. The lines were chosen based on their strength, blaze placement, and simplicity (i.e., no blends).

Table 4.7. Best-Fit Spectral Type Templates

Lines	$T_{\text{eff}}$ (K)	Primary		Secondary			$\chi_r^2$
		$\log g$	[Fe/H]	$T_{\text{eff}}$ (K)	$\log g$	[Fe/H]	
P	17000	4.0	-0.3	7500	3.0	-0.3	2.00
S	17000	5.0	-1.0	7000	5.0	-0.3	1.98
P & S	17000	4.0	-1.0	7000	5.0	-0.3	1.97

### 4.1.3 Constraint of Stellar Parameters

The sampled spectrum provided by the HET HRS of the primary and secondary stars of BM Ori was fed into the IDL spectral typing routine. Once a suitable fit was found, the  $\chi_r^2$  was calculated and saved to an array to be retrieved and analyzed later. After all 216 spectral combinations were fit for all 53 exposures, the minimum mean  $\chi_r^2$  was found.

Three versions of the spectral typing routines were performed to constrain the stellar parameters of the BM Ori components. First, the two strongest primary lines (see Table 4.5) had their normalized and truncated spectra stitched together and fed into the spectral typing routine developed by the author. The second version of the spectral typing routine instead used the ten strongest secondary lines (Table 4.6) to compare to synthetic templates. Lastly, all 12 lines had their regions stitched together to obtain a simultaneous fit.

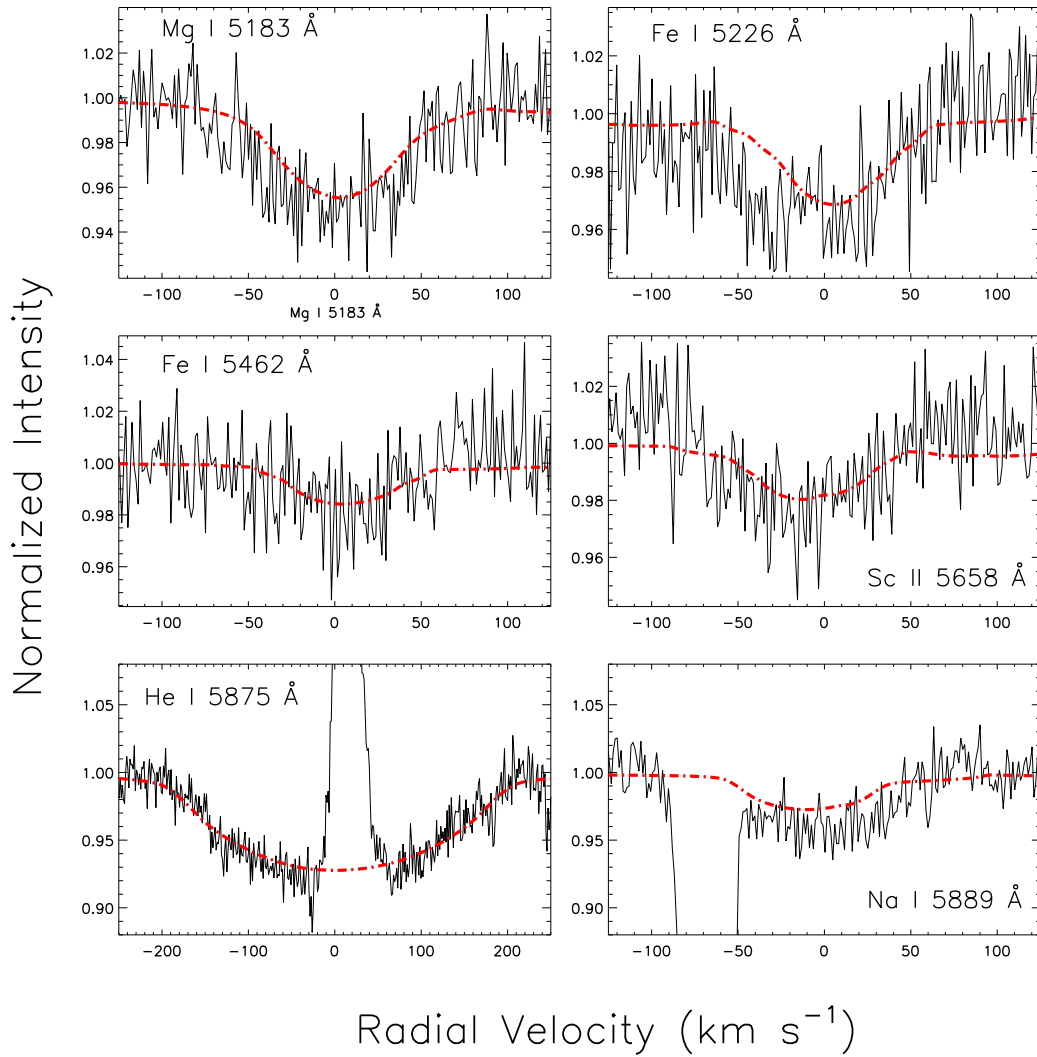
The best-fit spectrum combination for BM Ori's primary lines (He I 5875 Å and He I 6678 Å) was with a primary effective temperature of 17000 K,  $\log g$  of 4.0, and metallicity of -0.3 and secondary temperature of 7500 K,  $\log g$  of 3.0, and metallicity of -0.3. Interestingly, the best-fit spectrum combination for BM Ori's secondary lines was with a primary effective temperature of 17000 K,  $\log g$

of 5.0, and metallicity of  $-1.0$  and secondary temperature of 7000 K,  $\log g$  of 5.0, and metallicity of  $-0.3$ . A simultaneous fit of both primary and secondary features against spectral type resulted in a best-fit spectrum combination of primary effective temperature of 17000 K,  $\log g$  of 4.0, and metallicity of  $-1.0$  and secondary temperature of 7000 K,  $\log g$  of 5.0, and metallicity of  $-0.3$ . An example of this best-fit spectrum is shown in Figures 4.2 and 4.3. The agreement of both secondary and the primary and secondary line concatenations makes sense because of the number of secondary lines used in the fits compared to the 2 lines of the primary. Of note is the seemingly consistent agreement of 17,000 K, cooler than what has been determined previously.

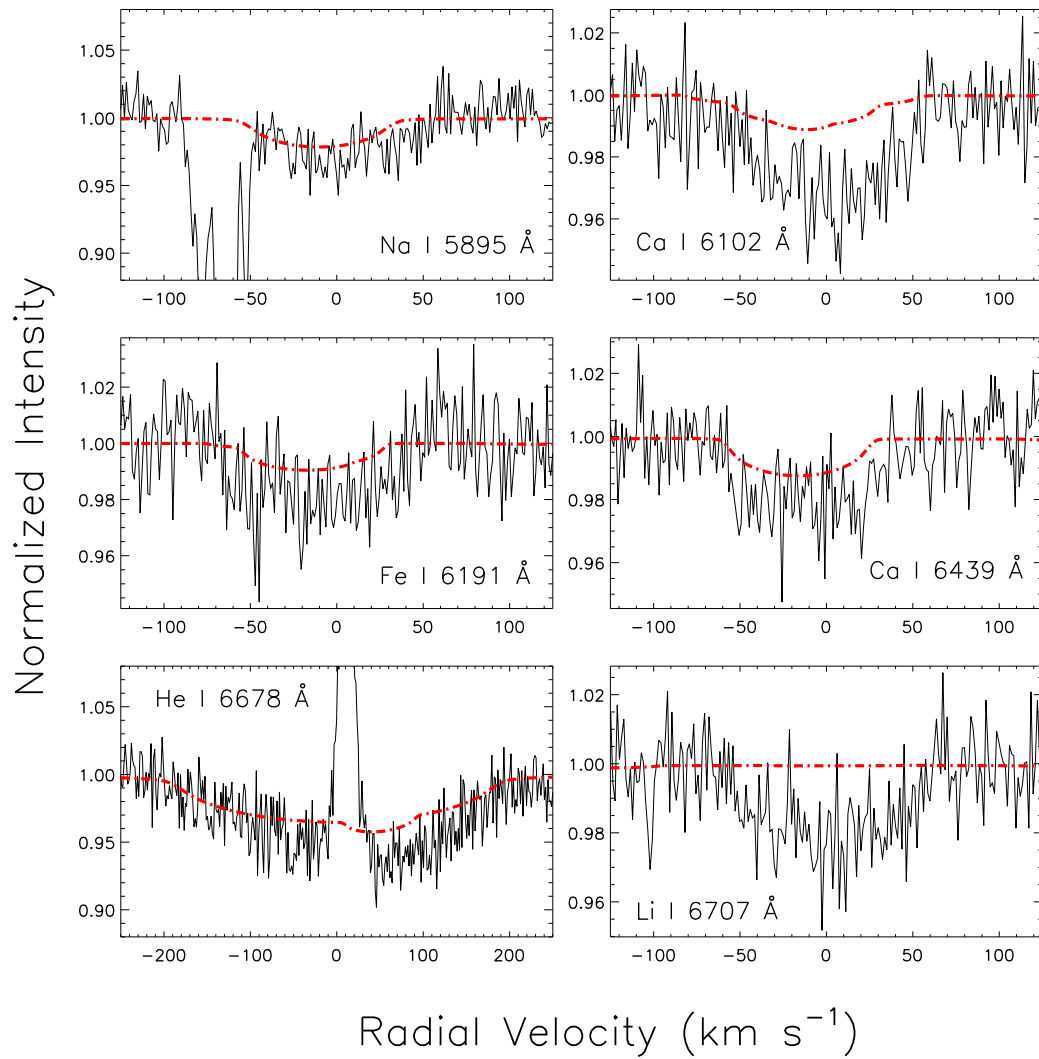
## 4.2 Rotational Velocity of the Components of BM Ori

Using the spectral types for the components of BM Ori, rotational velocity information could now be gleaned since one parameter that was allowed to vary was that of  $v \sin i$ . One output of the IDL spectral typing routine was a three-dimensional array containing the best-fit  $v \sin i$  parameters found for each exposure and stellar parameter combination. The final  $v \sin i$  for a BM Ori component was calculated by averaging the calculated  $v \sin i$  parameters for all exposures using the spectral combination that produced the minimum average  $\chi_r^2$ . For the primary, this rotation value is  $187 \text{ km s}^{-1}$  while for the secondary this value is  $42 \text{ km s}^{-1}$ . The final results are tabulated in Table 4.8.

Figures 4.4 and 4.5 show the  $v \sin i$  determinations as a function of phase using the best-fit spectral typing output for the primary and secondary stars.



**Figure 4.2:** Best-fit rotationally broadened template spectra overlaid on top of HET data. This particular exposure was hrs913319 at a phase of  $P=0.0453$ .



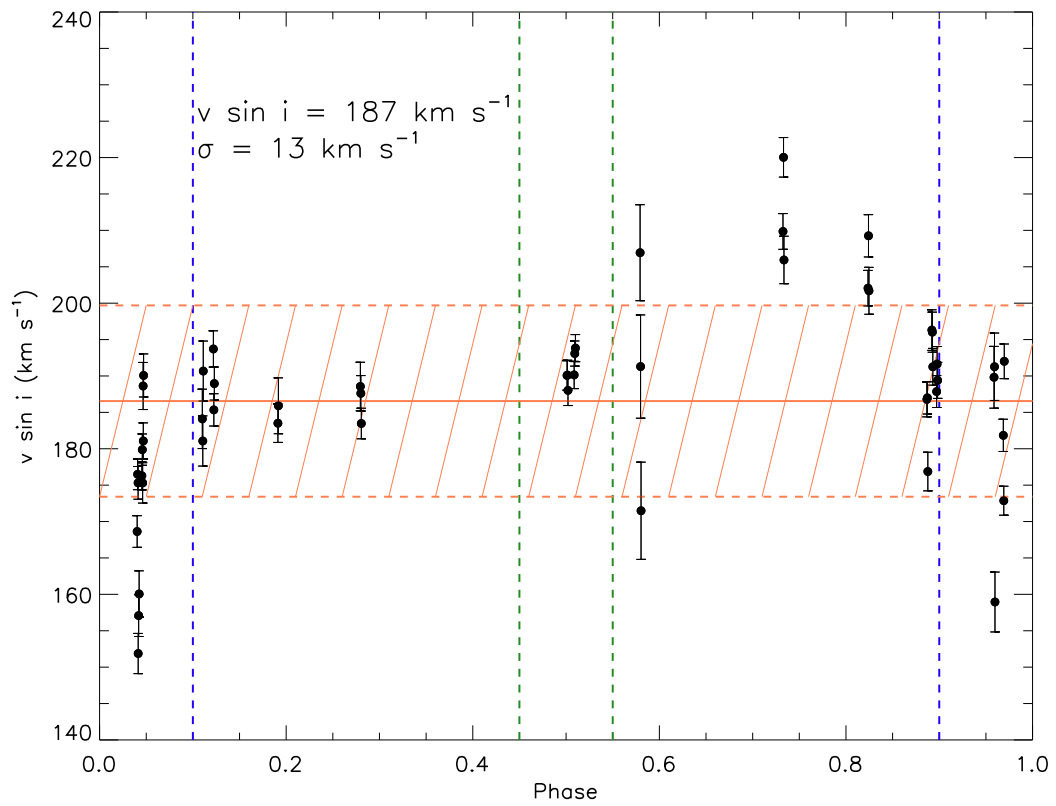
**Figure 4.3:** Best-fit rotationally broadened template spectra overlaid on top of HET data. This particular exposure was hrs913319 at a phase of  $P=0.0453$ .

Table 4.8. Rotation Parameters of BM Ori

Component	$v \sin i$ (km s <sup>-1</sup> )
Primary	187±13
Secondary	42±4

One can immediately see that in Figure 4.5 during secondary eclipse,  $v \sin i$  shows a dramatic increase. This is expected since this is the point in BM Ori's orbit where the secondary is occulted by the primary. No secondary lines should be visible, or if they are, should be quite weak. The increased  $v \sin i$  calculated at this phase is the fitting routine actually trying to flatten the template spectrum beneath the noise. These particular  $v \sin i$  results for the secondary were not used in the final calculation.

Another noticeable feature of Figures 4.4 and 4.5 occurs at a phase  $\sim 0.54$ . The spread in rotational velocities observed here is uncharacteristically large when compared to that of the other observations. When looking at the signal-to-noise ratios for these particular exposures (Table 3.1), one sees that this spread may be due to its low value compared to all other SNRs. Also, for the primary, there are a handful of points that are further from the mean than would be expected. Again, these particular exposures have low SNRs. Further research into the night reports for these observations (Dec. 23, 2008; Jan. 9–11, 2009; Feb. 25, 2009) show that while there were no indications of anything wrong with the exposures of BM Ori, clouds and bad seeing appeared throughout the night which may have plagued our data but gone undocumented.



**Figure 4.4:** Best-fit  $v \sin i$  parameters for the primary. Values are plotted against phase. Blue dashed lines indicate start and end of primary eclipse. Green dashed lines indicate start and end of secondary eclipse.

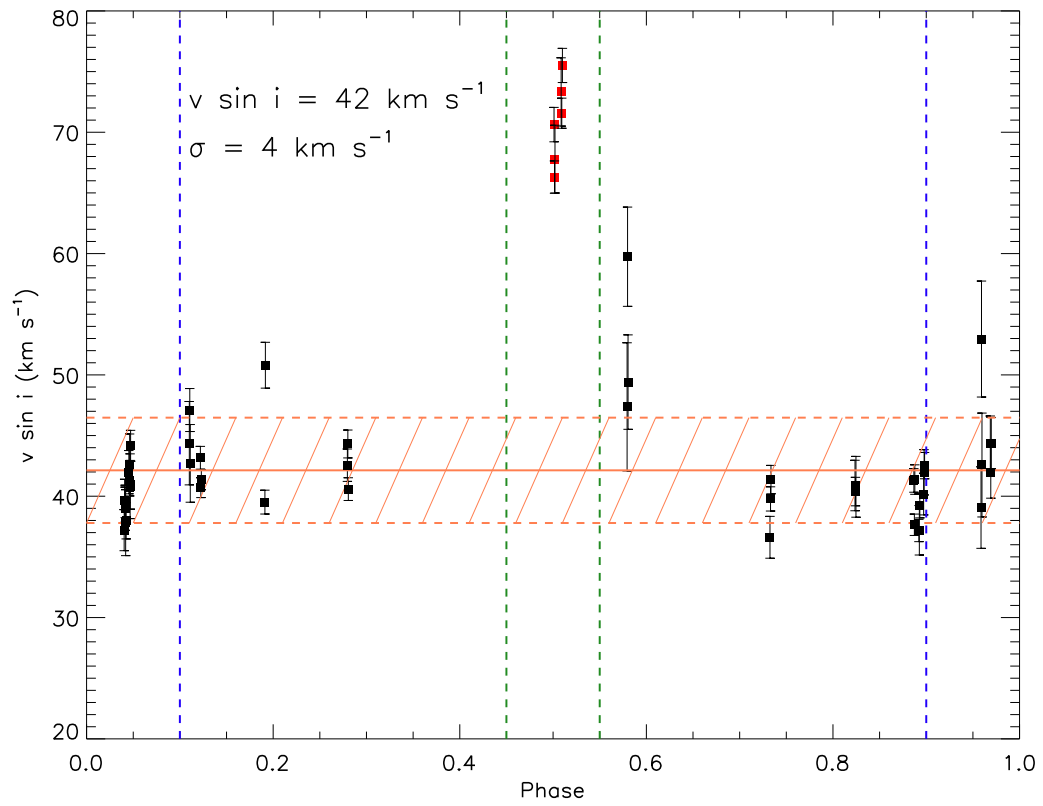


**Figure 4.5:** Best-fit  $v \sin i$  parameters for the secondary. Values are plotted against phase. Blue dashed lines indicate start and end of primary eclipse. Green dashed lines indicate start and end of secondary eclipse. Data points in red were not used to calculate the final  $v \sin i$ .

Table 4.9. Comparison of BM Ori Rotation Parameters from Literature

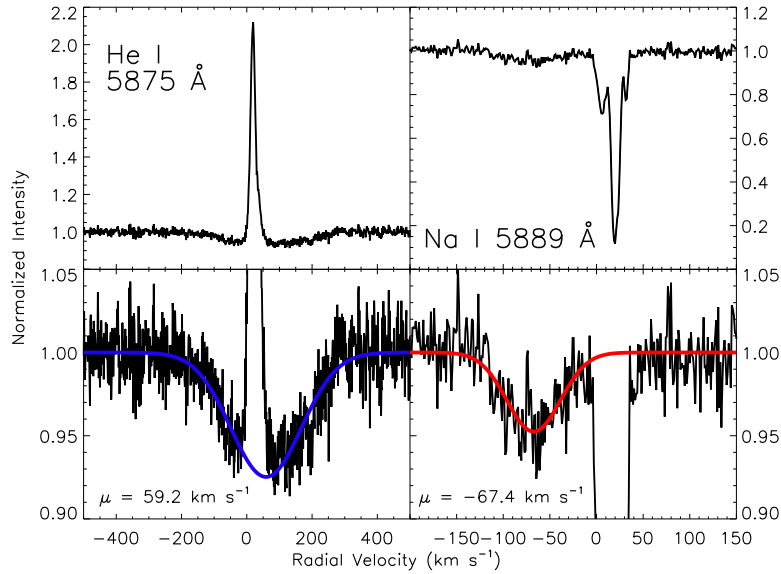
Author(s)	Primary $v \sin i$ (km s <sup>-1</sup> )	Secondary $v \sin i$ (km s <sup>-1</sup> )
Abt et al. (1970)	320±10	-
Popper & Plavec (1976)	-	50-100
Ismailov (1988)	150±40	-
Vitrichenko et al. (1996)	170±10	55±5
Vitrichenko & Plachinda (2000)	-	60±3
This work	187±13	42±4

Table 4.9 shows how the best-fit rotation parameters from the spectral typing routine compare with those determined in past literature. The primary rotation parameter is nicely in agreement with past calculations except for that of Abt et al. (1970). On the other hand, the  $v \sin i$  of the secondary does not seem to agree. Whether the secondary is slowing down, the previous measurements were overestimates, or the limited sample of stellar parameters is causing an underestimation of the actual  $v \sin i$  remains to be seen.

### 4.3 Refined Radial Velocity Curve

#### 4.3.1 Radial Velocity Curve via Gaussian Profile Fitting

Using the `mpfit` package, normalized and truncated spectra were fed into a procedure developed by the author to find the centroid of any identified absorption feature in velocity space (see Figure 4.6). Once fit, the mean, sigma, and equivalent width of the Gaussian profile were saved to a text file with the same information for all of the other exposures. This information was later accessed to produce radial velocity curves. Though not the best physical representation



**Figure 4.6:** Example Gaussian fit of the He I 5875 Å line of the primary and the Na I 5889 Å line of the secondary. The centroid of the Gaussian tells the radial velocity of the star at this particular phase.

of the absorption features, the Gaussian profile fitting was effective in producing clear radial velocity curves and narrowing the space over which future analyses would have to cover (see Sec. 3.1.2).

Figure 4.6 shows both nebular emission for the He I line and interstellar absorption for the Na I line. Both were extracted as explained in Sec. 3.1.3 to ensure the most precise Gaussian profile fit.

At early stages in this project, the orbital parameters of BM Ori were going to be solely determined by the information gleaned from Gaussian profile fits of all absorption features. The radial velocity curve generated by these data is shown in Figure 4.7. Data points were generated by averaging all radial velocity measurements determined from all of the component’s lines for each night. The standard deviation of these measurements are plotted as the error bars. Using a sine curve (i.e., eccentricity of zero) to fit the primary and secondary data individ-

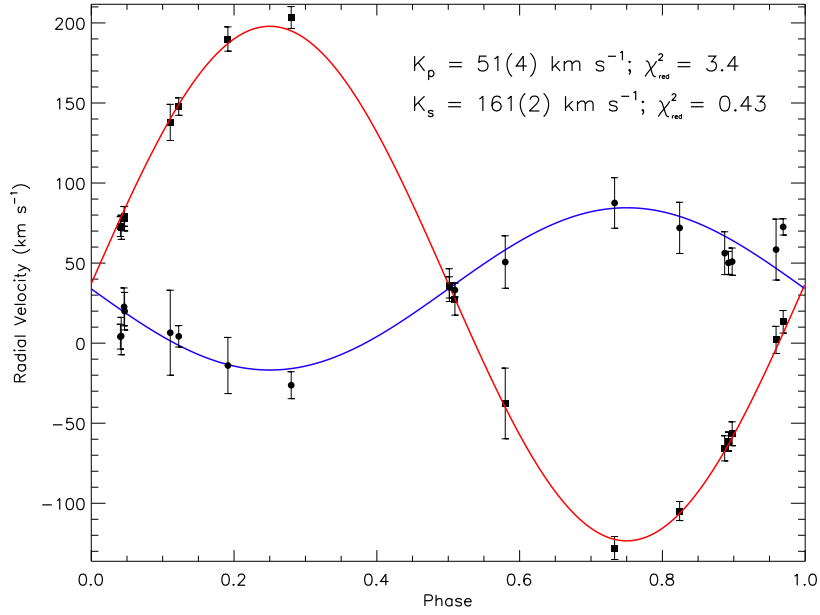


**Figure 4.7:** Refined radial velocity curve using Gaussian profiles of absorption features. Error bars represent standard deviation of radial velocities measurement for all lines on a single night.

Table 4.10. Orbital Parameters of Radial Velocity Curve Generated By Gaussian Profile Fitting Routine

Component	$K$ (km s <sup>-1</sup> )	$\gamma$ (km s <sup>-1</sup> )	$\chi_r^2$
Primary	51±4	34±2	3.4
Secondary	161±2	37±2	0.43

ually, a velocity semi-amplitude of the primary component was determined to be  $51 \pm 4 \text{ km s}^{-1}$  while the secondary component has a velocity semi-amplitude of  $161 \pm 2 \text{ km s}^{-1}$ . A summary of the orbital parameters are given in Table 4.10.

### 4.3.2 Radial Velocity Curve via Spectral Typing

The process of spectral typing both the primary and secondary stars of BM Ori simultaneously required that parameters be incorporated into the routine that represented the radial velocity shifts of the respective spectra. Using these best-fit parameters, a radial velocity curve was generated (see Figure 4.8). Again, using the functional form of a sine wave, the velocity semi-amplitudes found using the radial velocities gleaned from the spectral typing process were  $59 \pm 2 \text{ km s}^{-1}$  for the primary while the secondary component has a velocity semi-amplitude of  $174 \pm 1 \text{ km s}^{-1}$ .

The larger reduced chi squared observed with this radial velocity curve may be a byproduct of the error propagation of `mpfitexpr.pro`. The `mpfit` package uses standard error propagation techniques to provide formal  $1\text{-}\sigma$  uncertainties on fitted parameters by taking the square root of the covariance matrix. In general these approaches will underestimate the actual error. This was observed for the radial velocity curve using Gaussian profiles and was circumvented by the use of the standard deviation due to the numerous measurements of radial velocity which occurred simultaneously from every identified line of BM Ori. In the spectral typing routine, essentially all lines were treated as one measurement to determine the rotational broadening and radial velocity for a specific spectral type, thus decreasing our number of measured velocities by a factor of 12. For the radial velocity curve created from the best-fit parameters of the spectral typing routine,

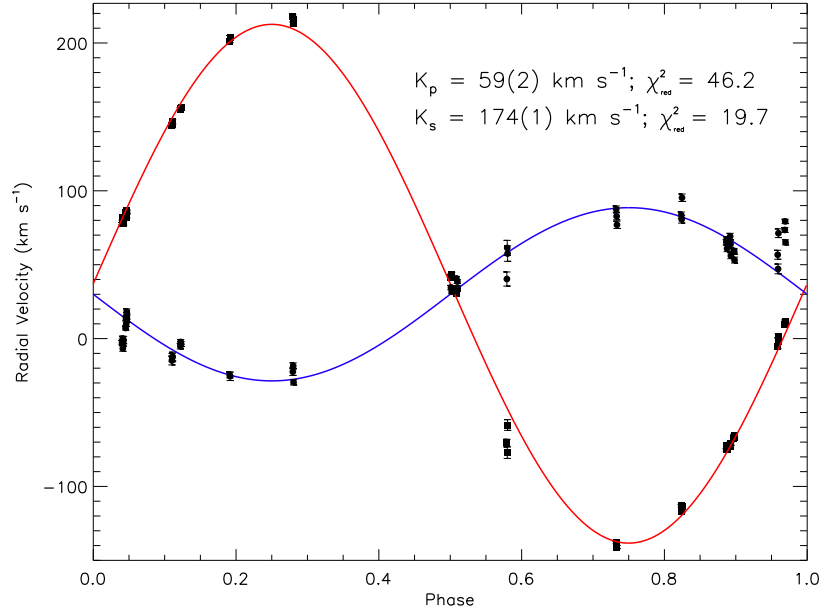


**Figure 4.8:** Refined radial velocity curve using best-fit rotation parameters.

Table 4.11. Orbital Parameters of Radial Velocity Curve Generated Using Spectral Typing Routine

Component	$K$ ( $\text{km s}^{-1}$ )	$\gamma$ ( $\text{km s}^{-1}$ )	$\chi_r^2$
Primary	$59 \pm 2$	$31 \pm 2$	46.2
Secondary	$174 \pm 1$	$38 \pm 1$	19.7

a boot strap analysis was performed to estimate the  $1\sigma$  uncertainties in the systemic velocity and velocity semi-amplitude. These errors are reported in Figure 4.8 and Table 4.11.

### 4.3.3 Eccentricity Consideration

For both the Gaussian profile and rotational broadening radial velocity curves, a routine was developed to determine if there was any hint of eccentricity in the orbit of BM Ori. This IDL routine created by the author solved Kepler's Equation

$$M = E - e \sin E \quad (4.2)$$

where  $M$  is the mean anomaly of the BM Ori orbit,  $E$  is the eccentric anomaly of the BM Ori orbit, and  $e$  is the orbit's eccentricity. The transcendental nature of Kepler's equation requires an iterative process for convergence. To speed up the eccentricity determination, a small parameter space of eccentricities ranging from 0.0 to 0.2 in increments of 0.01 was used. The solver found that the  $\chi^2$  of the radial velocity curve was minimized with an eccentricity of zero for the radial velocity curve generated with Gaussian profiles centroids. Using the velocity semi-amplitude of the secondary star from the radial velocity curve generated by the results of the spectral typing routine, the solver found that the  $\chi^2$  of the radial velocity curve was minimized with an eccentricity of 0.02. It must be noted here that due to the small number of data points and errors bars resulting from the `mpfit` package, the eccentricity determination needs more assessment before declaring this a true result. The solver developed by the author assumed a value for the velocity semi-amplitude provided by the user that did not vary. There may be potential to use this Kepler equation solver to search a range of amplitudes so

that it can also obtain all of the orbital parameters of BM Ori that pertain to the radial velocity curve.

## 4.4 Mass Ratio

The mass ratio of BM Ori’s primary to secondary can be determined by the velocity semi-amplitudes as determined by the radial velocity curve via the relation

$$\frac{M_1}{M_2} = \frac{K_2}{K_1}. \quad (4.3)$$

While the two methods’ velocity semi-amplitudes do not agree within errors (most likely due to an underestimation of errors for the rotationally broadened radial velocity curve), the mass ratios do agree as summarized in Table 4.12. In addition, both are consistent with the original Popper & Plavec (1976) values.

A summary of orbital parameters determined previously are presented in Table 4.13. The orbital parameters found in this work agree to various degrees with previous findings. The key factor it seems is the representation of errors. For instance, the only reason our model for the secondary agrees with the findings of Popper & Plavec (1976) is because of their estimation of their uncertainty of  $10 \text{ km s}^{-1}$  after deeming their original  $1\sigma$  errors too small. In a similar vein, our estimates of the parameter uncertainties were lower than expected and we invoked reasonable methods (i.e., using the standard deviation of all measurements, bootstrap analysis) to produce numbers that reflected the true errors in our observations. Better understanding of the calculation of errors by the `mpfit` package could lessen our reliance on other error estimation methods.

Another noticeable difference between the current work’s best-fit orbital pa-

Table 4.12. Mass Ratio of BM Ori Primary to Secondary

Method	Mass Ratio
Gaussian	$3.17 \pm 0.27$
Rotation	$2.94 \pm 0.03$

rameters and those found in literature is the seemingly significant increased systemic velocity of the BM Ori system. This difference is as much as  $23 \text{ km s}^{-1}$ . It is unclear where this large difference can be attributed to but further exploration in error calculations and radial velocity curve fitting models is necessary to resolve this discrepancy.

Table 4.13. BM Ori Orbital Parameters from Literature

Author(s)	$K_p$ (km s <sup>-1</sup> )	$\gamma_p$ (km s <sup>-1</sup> )	$K_s$ (km s <sup>-1</sup> )	$\gamma_s$ (km s <sup>-1</sup> )	$\frac{M_1}{M_2}$
Popper & Plavec (1976)	52.8±2.1	20.7±1.6	171±10	23.6±3.8	3.24±0.23
Vitrichenko et al. (1996)	66±3	15±2	170±3	15±2	2.58±0.13
This work <sup>a</sup>	51±4	34±2	161±2	37±2	3.17±0.27
This work <sup>b</sup>	59±2	31±2	174±1	38±1	2.94±0.03

<sup>a</sup>Orbital parameters determined by fitting of Gaussian profiles.

<sup>b</sup>Orbital parameters determined by spectral type fitting.

# Chapter 5

## Fitting the Puzzle Pieces Together

### 5.1 Summary of Results

Using a grid of 216 stellar parameter combinations, the spectral type of the BM Ori secondary was found to be consistent with a 7000 K effective temperature,  $\log g$  of 5.0, and  $[\text{Fe}/\text{H}] = -0.3$ , F2 star. The primary star was found to be consistent with a 17,000 K effective temperature,  $\log g$  of 4.0, and  $[\text{Fe}/\text{H}] = -1.0$ , B4 star. The coarse grid and discrete intervals of  $\log g$  and  $[\text{Fe}/\text{H}]$  in the BLUERED synthetic spectra templates make it difficult to assign appropriate error bars to the best-fit spectral type combination found in this project. One might think the discrepant metallicities suggest that perhaps the two components of BM Ori are not coeval or that material from the disk surrounding the secondary might be falling onto the secondary star, increasing its metallicity. Such judgments would be hasty due to the small number of parameters surveyed by the time of this writing and lack of error estimates. A possible trend can be seen in that the lowest  $\chi_r^2$  resulted from secondary stellar parameter combinations with increased metallicities, as seen in Table 5.1.

Using two different methods for finding radial velocity, the mass ratio of primary to secondary was found to be  $3.17 \pm 0.27$  (via Gaussian profile fitting) and  $2.94 \pm 0.03$  (via spectral typing) in accordance with previous findings. Though the

Table 5.1. Sample Grid of  $\chi_r^2$  Values Obtained from Spectral Typing Routine

S \ P	t17000g40m10 <sup>a</sup>	t17000g50m10	t17000g40m03	t17000g50m03
t07000g30m10	2.043	2.049	2.049	2.049
t07000g40m10	2.040	2.047	2.046	2.046
t07000g50m10	2.028	2.034	2.035	2.034
t07000g30m03	1.995	2.001	2.029	2.024
t07000g40m03	1.981	1.987	2.014	2.010
t07000g50m03	1.966	1.972	2.002	1.997

<sup>a</sup>Naming scheme is as described in Sec. 4.1.

two methods' velocity semi-amplitudes did not agree within errors, this is most likely due to the underestimate of parameter uncertainties using the robust, least-squares fitting routine `mpfit`. The systemic velocities found by zero eccentricity orbits agreed within errors. Future work may consider a better estimation of the uncertainty of parameters calculated via the spectral typing routine so that the two methods (Gaussian profiles and rotational broadening) can be consistent with each other.

## 5.2 Other Idiosyncrasies of BM Ori and Future Work

Though this project comes to a close, much more work can be done with the rich HET data set. Some interesting points identified but not fully explained nor understood by the time of this writing are discussed below.

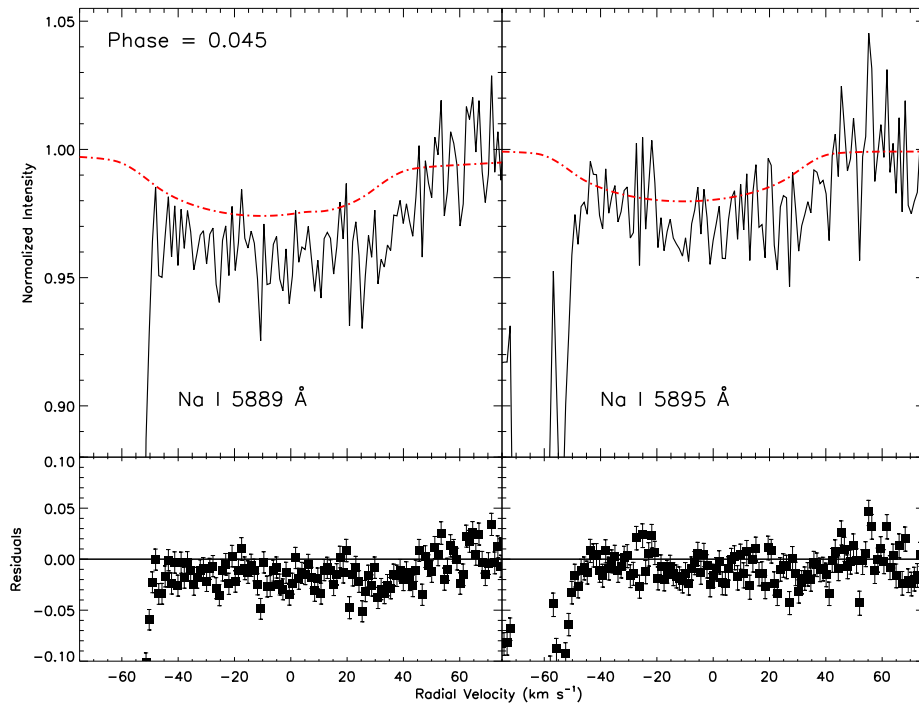


**Figure 5.1:** HET data with best-fit rotationally broadened spectrum overlaid on top of it, zoomed in on the Na I doublet region. An interstellar absorption feature ends in both panels at around  $-50 \text{ km s}^{-1}$ . The residuals show no sharp excess features that would be indicative of excess, cool sodium in the disk surrounding the secondary star.

### 5.2.1 Search for Sodium Excess

With better constraints on the spectral types of the components of BM Ori comes enhanced ability to check for excess metal absorption. The presence of excess absorption would manifest itself as a sharp feature due to the cooler nature of any dust or gas further away from the secondary star. Analysis of 18 exposures during ingress and egress showed no significant extra absorption features. Any appearance of an extra absorption could not be differentiated from noise. In addition, no complementary excess absorption was evident in the second Na I doublet line. For an example of such residuals, see Figure 5.1.

Broad excess absorption is apparent in Figure 5.1 but this may be due to the best-fit stellar parameters found for the BM Ori components in this project not precisely describing the system. Additionally, decreased dilution by the primary would also account for the observed offset. Future spectral typing routines will need to account for the percentage of the primary disk that is blocked by the secondary so that more accurate flux ratios can be used when minimizing the  $\chi^2$  statistics of the fits.

### 5.2.2 Presence of Lithium in BM Ori Spectrum

The presence of Li I 6707 Å in the secondary and its absence in any of the spectral templates may be an excellent indicator of BM Ori's youth. Some amount of lithium was present in all exposures so that it could generate its own radial velocity curve using the Gaussian profile technique. The absorption of Li I 6707 Å is more pronounced during primary eclipse, an example of which is shown in Figure 5.2. Calculating the exact abundance goes beyond the scope of this project, but will be conducted in the near future to constrain the age of the BM Ori system

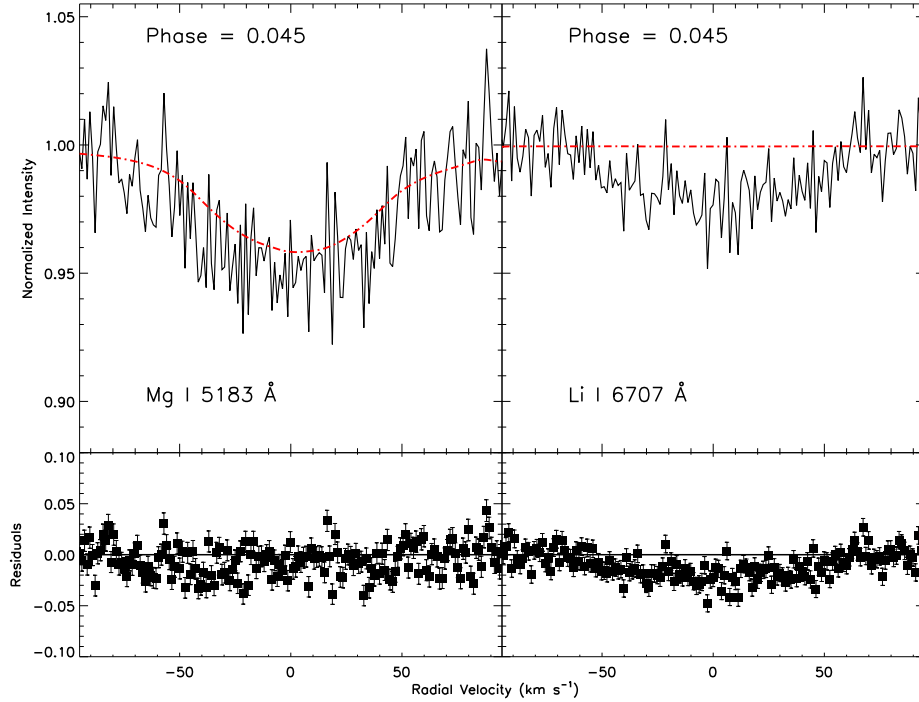


**Figure 5.2:** Comparison of Mg I 5183 Å line of secondary to that of Li I 6707 Å. The best-fit broadened spectral template combination is overlaid on top of the HET data.

and see if it agrees with the contraction ages determined by Palla & Stahler (2001).

### 5.2.3 Overabundance of Ca I 6102 Å and Ca I 6439 Å in BM Ori Spectrum

While lithium may lead to further constraint of BM Ori’s age, the apparent overabundance of Ca I 6102 Å and Ca I 6349 Å may hint at a peculiar metallicity of the secondary component of BM Ori. As with the Li 6707 Å line, the strength of the lines appear greatest during primary eclipse phases, a phase which is shown in Figure 5.3.

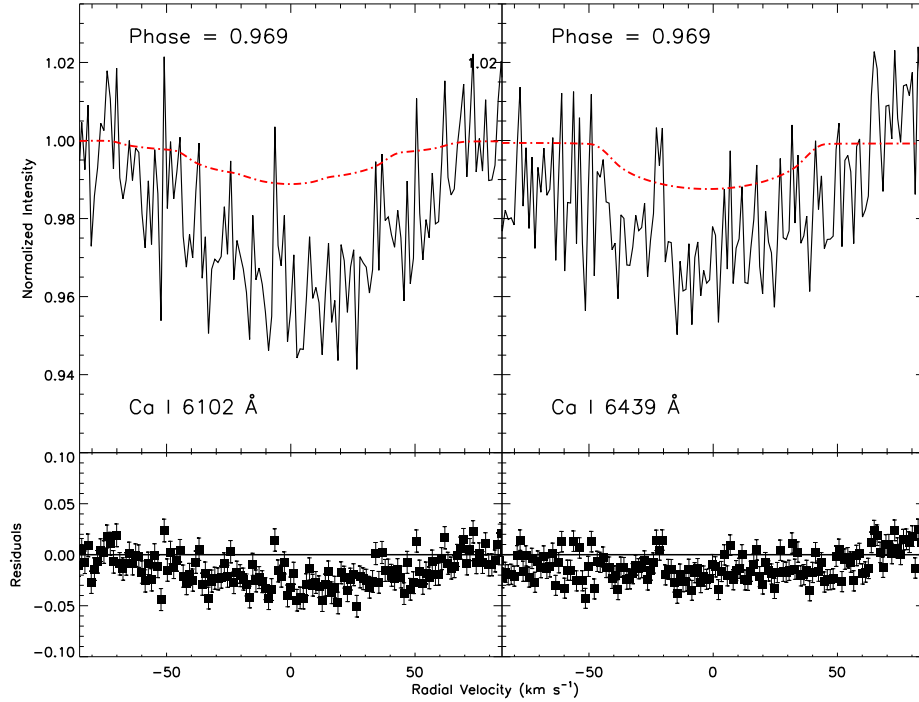


**Figure 5.3:** Example exposure of the two calcium lines detected in the BM Ori spectra. This “bad” fit is characteristic of all exposures in our data set.

### 5.2.4 H $\alpha$

The H $\alpha$  region was difficult to scrutinize due to strong nebular emission and BM Ori’s stellar absorption. Normalizing the spectra and then utilizing the Gaussian profile fitting routine was not adequate for obtaining accurate radial velocity information. Even though this region was not used to produce the refined radial velocity curves, H $\alpha$  became of interest when intensity variations located at the intersection of the nebular emission and stellar absorption were noticed (see Figure 5.4). Two protrusions are seen on either side of the large emission feature. When different exposures were examined, these “feet” seemed to move. In an attempt to discern whether this variability is due to the Orion Nebula or BM Ori

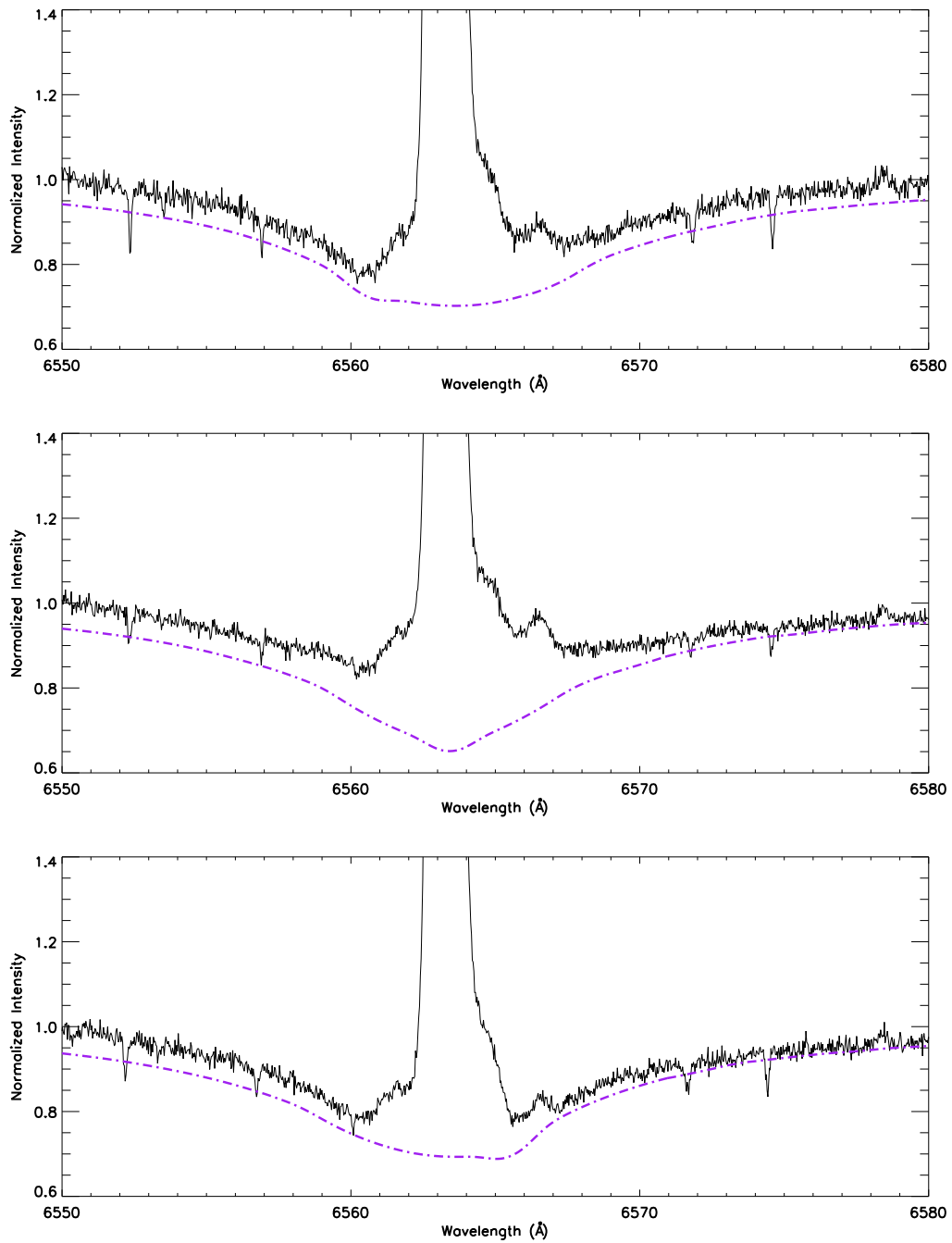


**Figure 5.4:** A sample of the “variability” of the  $H\alpha$  line. The intensity variations of the “feet” surrounding the line coincide with the presence of BM Ori’s hydrogen absorption. The purple dash-dot line is the best-fit model of the primary and secondary of BM Ori found using the spectral typing routine.

itself, the best-fit spectral templates of the primary and secondary were used to model the deep absorption of the BM Ori system. One can see that the change in intensity of these feet correspond to the asymmetrical H $\alpha$  absorption from both of BM Ori's components. This still leaves the question of what these protrusions actually are. Some speculation is that they are evidence of accretion or a wind. These features are not reminiscent of P Cygni features. There is an asymmetry present but the asymmetry is that of emission, not blue-shifted absorption and red-shifted emission. It appears that as the BM Ori system moves, the nebular emission of H $\alpha$  is slightly attenuated.

### 5.2.5 Refined Spectral Typing

Computation time was a significant factor in the limited spectral type grid that was considered for this project. There are plans to expand this parameter space and include more effective temperatures of the primary and secondary, in addition to the  $\log g$  and [Fe/H] stellar parameters. Finer gradations of these parameters can only help to further constrain the spectral types of both components of BM Ori and develop proper errors. Since H $\alpha$  is such a strong feature that dominates the spectra, it may also be incorporated into the spectral typing routine to better assess the component temperatures of the system. Vitrichenko & Tsymbal (1996) even speculated that an apparent excess of intensity could be attributed to radiating material surrounding the secondary, a method the author is eager to explore.

### 5.2.6 Continued Observation

Although the phase coverage of BM Ori by the HET data set was impressive, some factors outside the control of the author impeded its interpretation and analysis. Most notable was the lack of zero phase coverage during the primary eclipse. Exposures taken during ingress and egress were not enough to capture a hint of potential excess sodium absorption, nor could it definitively be ruled out. Additionally the “shoulders” just before and after primary and secondary eclipse were also inconclusive, owing to decreased SNRs from bad seeing and clouds during the time of observation. As Popper & Plavec (1976) alluded to in the title of their 1976 paper, the enigmatic nature of BM Ori may not have been completely understood by the end of this project, but steps have and will soon be taken to fit its different facets together so that a clearer physical picture of this system can emerge.

# Bibliography

- Abt, H. A., Muncaster, G. W., & Thompson, L. A. 1970, *AJ*, 75, 1095
- Al-Naimiy, H. M. K., & Al-Sikab, A. O. 1984, *Ap&SS*, 103, 115
- Antokhina, E. A., Ismailov, N. Z., & Cherepashchuk, A. M. 1989, *Soviet Astronomy Letters*, 15, 362
- Bally, J., Sutherland, R. S., Devine, D., & Johnstone, D. 1998, *AJ*, 116, 293
- Bertone, E., Buzzoni, A., Chávez, M., & Rodríguez-Merino, L. H. 2008, *A&A*, 485, 823
- Bondar', N. I., & Vitrichenko, E. A. 1995, *Astronomy Letters*, 21, 627
- Close, L. M., Puglisi, A., Males, J. R., Arcidiacono, C., Skemer, A., Guerra, J. C., Busoni, L., Brusa, G., Pinna, E., Miller, D. L., Riccardi, A., McCarthy, D. W., Xompero, M., Kulesa, C., Quiros-Pacheco, F., Argomedo, J., Brynnel, J., Esposito, S., Mannucci, F., Boutsia, K., Fini, L., Thompson, D. J., Hill, J. M., Woodward, C. E., Briguglio, R., Rodigas, T. J., Briguglio, R., Stefanini, P., Agapito, G., Hinz, P., Follette, K., & Green, R. 2012, *ApJ*, 749, 180
- Cuntz, M. 2013, ArXiv e-prints
- Dvorak, R. 1982, *Oesterreichische Akademie Wissenschaften Mathematisch naturwissenschaftliche Klasse Sitzungsberichte Abteilung*, 191, 423
- Eggl, S., Pilat-Lohinger, E., Georgakarakos, N., Gyergyovits, M., & Funk, B. 2012, *ApJ*, 752, 74

- Esteban, C., Peimbert, M., García-Rojas, J., Ruiz, M. T., Peimbert, A., & Rodríguez, M. 2004, *MNRAS*, 355, 229
- Galileo, G. 1617, *Le Opere di Galileo*
- Goos, F. 1918, *Astronomische Nachrichten*, 207, 15
- Gray, D. F. 2008, *The Observation and Analysis of Stellar Photospheres*
- Hall, D. S., & Garrison, Jr., L. M. 1969, *PASP*, 81, 771
- Hartwig, E. 1921, *Astronomische Nachrichten*, 212, 383
- Huygens, C. 1659, *Systema Saturnia*
- Ismailov, N. Z. 1988, *Soviet Astronomy Letters*, 14, 138
- Kiseleva-Eggleton, L., & Eggleton, P. P. 2001, in *Astronomical Society of the Pacific Conference Series*, Vol. 229, *Evolution of Binary and Multiple Star Systems*, ed. P. Podsiadlowski, S. Rappaport, A. R. King, F. D'Antona, & L. Burderi, 91
- Kramida, A., Ralchenko, Y., & Reader, J. 2012
- Lobel, A. 2007, in *UV Astronomy: Stars from Birth to Death*, ed. A. I. Gómez de Castro & M. A. Barstow, 167
- Markwardt, C. B. 2009, in *Astronomical Society of the Pacific Conference Series*, Vol. 411, *Astronomical Data Analysis Software and Systems XVIII*, ed. D. A. Bohlender, D. Durand, & P. Dowler, 251
- McCaughrean, M. J., & Stauffer, J. R. 1994, *AJ*, 108, 1382
- Palacios, A., Gebran, M., Josselin, E., Martins, F., Plez, B., Belmas, M., & Lèbre, A. 2010, *A&A*, 516, A13

- Palla, F., & Stahler, S. W. 2001, *ApJ*, 553, 299
- Pope, T., & Mosher, J. 2006
- Popper, D. M., & Plavec, M. 1976, *ApJ*, 205, 462
- Schneider, J., Dedieu, C., Le Sidaner, P., Savalle, R., & Zolotukhin, I. 2011, *A&A*, 532, A79
- Schneller, H. 1940, *Kleine Veroeffentlichungen der Universitaetssternwarte zu Berlin Babelsberg*, 5, 2
- Struve, O., & Titus, J. 1944, *ApJ*, 99, 84
- Vasileiskii, A. S., & Vitrichenko, E. A. 2000, *Astronomy Letters*, 26, 529
- Vitrichenko, E. A. 2005, *Astrophysics*, 48, 475
- Vitrichenko, E. A., & Klochkova, V. G. 2001, *Astronomy Letters*, 27, 328
- . 2004, *Astrophysics*, 47, 169
- Vitrichenko, É. A., Klochkova, V. G., & Tsymbal, V. V. 2006, *Astrophysics*, 49, 96
- Vitrichenko, E. A., & Larionov, V. M. 1996, *Astronomy Letters*, 22, 157
- Vitrichenko, E. A., & Plachinda, S. I. 2000, *Astronomy Letters*, 26, 390
- Vitrichenko, E. A., Shevchenko, V. S., & Shcherbakov, V. A. 1996, *Astronomy Letters*, 22, 163
- Vitrichenko, E. A., & Tsymbal, V. V. 1996, *Astronomy Letters*, 22, 116
- Wilson, R. E. 1972, *Ap&SS*, 19, 165

Windemuth, D., Herbst, W., Tingle, E., Fuechsl, R., Kilgard, R., Pinette, M.,  
Templeton, M., & Henden, A. 2013, *ApJ*, 768, 67

Wolf, G. W. 1994, *Experimental Astronomy*, 5, 61

Zakirov, M. M., & Shevchenko, V. S. 1982, *Peremennye Zvezdy*, 21, 638